Journal of Molecular Structure 1252 (2022) 131974

Contents lists available at ScienceDirect

Journal of Molecular Structure

journal homepage: www.elsevier.com/locate/molstr

Synthesis & characterization of heterocyclic disazo - azomethine dyes and investigating their molecular docking & dynamics properties on acetylcholine esterase (AChE), heat shock protein (HSP90α), nicotinamide *N*-methyl transferase (NNMT) and SARS-CoV-2 (2019-nCoV, COVID-19) main protease (M^{pro})

Hakki Yasin Odabasoglu[a,*], Taner Erdogan[b], Fikret Karci[c]

[a] *R&D Department, Hayat Kimya AS, Kocaeli, 41250, Turkey*
[b] *Department of Chemistry and Chemical Processing Technologies, Kocaeli Vocational School, Kocaeli University, Kocaeli, 41140, Turkey*
[c] *Department of Chemistry, Faculty of Science-Arts, Pamukkale University, Denizli, 20017, Turkey*

ARTICLE INFO

Article history:
Received 24 July 2021
Revised 1 November 2021
Accepted 19 November 2021
Available online 1 December 2021

Keywords:
Heterocyclic dye
Disazo-azomethine dye
Molecular docking
Molecular dynamics simulation
Binding affinity
SARS-CoV-2 main protease

ABSTRACT

In the study, by using 5-amino-4-arylazo-3-methyl-*1H*-pyrazole derivatives and 2–hydroxy-5-(phenyldiazenyl) benzaldehyde; eight novel heterocyclic disperse disazo-azomethine dyes were synthesized, their chemical structures were characterized via FT-IR and ^{1}H NMR studies. Synthesized compounds were also investigated computationally by performing various techniques. In the computational part of the study, geometry optimizations, frequency analyses, frontier molecular orbital (FMO) calculations, molecular electrostatic potential (MEP) map calculations, FT-IR and NMR spectral analyses were performed on the compounds. Additionally, to reveal their potentials against SARS-CoV-2 main protease (SARS-CoV-2 M^{pro}), acetylcholine esterase (AChE), heat shock protein (HSP90α) and nicotinamide *N*-methyl transferase (NNMT), molecular docking calculations were also performed on the synthesized compounds. Molecular dynamics (MD) simulations were carried out on the top-scoring ligand-receptor complexes to evaluate the stability of the complexes and the interactions between ligands and receptors in more detail. Results showed that synthesized compounds can interact with all these four receptors effectively and can be promising structures for further studies.

1. Introduction

Although the main usage of azo dyes is the dyeing of textile fabrics, there are many uses such as in liquid crystalline displays, computational studies, electro-optical devices, inkjet printers, solar cells, biological–medical studies, photo-sensitizers, photochromic materials and metallochromic indicators [1–10]. Researches show that these compounds can be used as antibacterial, antifungal, antitumor, antioxidant agents due to their broad range of pharmacological and medical potential [11–16].

Schiff bases were first synthesized by the German chemist Hugo Schiff in 1864. They are also named as azomethine compounds due to their CH=N group in their structure. Schiff bases, like azo dyes, have wide usage areas from textile dyeing to pharmacology even in vulcanization of rubber [17–21].

Lately azo-azomethine compounds are gaining interest due to their printing system properties and biological-medical studies [22–24]. Therefore, several studies have been published on the synthesis and spectral properties of azo-azomethine dyes [4,25–30].

From December 2019, Coronavirus disease-19 (2019-nCoV, COVID-19) is still spreading all over the world causing many deaths. Although there are vaccines developed and under development against COVID-19, there is no drug developed against this disease yet. Although some approved drugs currently on the market (e.g., remdesivir which is the only Food and Drug Administration-approved drug for the treatment of COVID-19 till now) are used to reduce the effects of COVID-19, there is a need to develop new specific drugs for this disease and will likely be in the future, too.

One of the potential targets for the treatment of this disease is SARS-CoV-2 M^{pro}. Playing a key role in viral replication and transcription [31] makes SARS-CoV-2 M^{pro} a promising target for drug development studies against COVID-19. Therefore, chemical com-

* Corresponding author.
E-mail address: yodabasoglu@hayat.com.tr (H.Y. Odabasoglu).

https://doi.org/10.1016/j.molstruc.2021.131974
0022-2860/

pounds that effectively interact with the active site of the enzyme can inhibit SARS-CoV-2 M^{pro} and thus can be a potential treatment for COVID-19. In the literature, there is some recent studies on the inhibition of SARS-CoV-2 M^{pro} [32–37].

In the present study, eight heterocyclic disperse disazo-azomethine dyes were synthesized by condensation of 5-amino-4-arylazo-3-methyl-*1H*-pyrazoles and 2–hydroxy-5-(phenyldiazenyl) benzaldehyde. Their structures were characterized by FT-IR, ^{1}H NMR, elemental analysis and computational studies were performed on synthesized compounds.

In the study, it was aimed to investigate the pharmaceutical potentials of the synthesized compounds computationally. For this purpose, reverse docking screening was performed for each compound. It was observed that the highest binding affinity was obtained for NNMT. Thus, molecular docking calculations and molecular dynamics simulations were performed for synthesized compounds and NNMT. In addition to NNMT, since AChE, HSP90α and especially SARS-CoV-2 M^{pro} are attractive targets for the treatment of Alzheimer's disease (AD), cancer and COVID-19, respectively, it was aimed to investigate the inhibition potentials of the synthesized compounds for these targets with the assistance of computational tools. The above-mentioned diseases, including COVID-19, which is affecting the whole world nowadays, are still important diseases without a complete cure, and new potential drugs need to be proposed for their treatment.

One of the aims of this study is to investigate whether the synthesized compounds can effectively interact with SARS-CoV-2 M^{pro} theoretically. Furthermore, to reveal their potentials against Alzheimer's disease and cancer it was also investigated that how the synthesized molecules interact with AChE and HSP90α through computational studies. As it is well known, Alzheimer's disease is a neurological disease that develops in the form of memory loss, dementia and decreased cognitive functions due to the death of brain cells over time. Today, the most effective therapeutic approach for the treatment of AD is inhibiting AChE. Inhibiting this enzyme leads to an increase in the acetylcholine level in brain. The main drugs for controlling the AD are galantamine, rivastigmine and donepezil. Since the selective AChE inhibitors have positive therapeutic effects on the disease, it is important to develop new selective AChE inhibitors to overcome this disease.

On the other hand, it is known that HSP90α is highly expressed in most tumor cells and plays a key role in the proliferation, malignant transformation, and progression of cancer cells. Currently, most HSP90α inhibitors under clinical evaluation act by blocking the binding of ATP to the HSP90α N-terminal domain and thereby, induce the degradation of many HSP90α-dependent on co-proteins [38].

Since the development of effective HSP90α inhibitors could make important contributions to cancer research, another aim of this study was to demonstrate the HSP90α inhibition potential of the synthesized compounds. In addition to AChE, HSP90α and SARS-CoV-2 M^{pro}, since the inverse docking calculations performed in the study showed that synthesized compounds can effectively interact with NNMT, molecular docking and MD simulation studies were also performed for the synthesized compounds and NNMT. NNMT is an enzyme which catalyzes the transfer of methyl group from S-adenosyl-L-methionine to nicotinamide to form N-methylnicotinamide and S-adenosyl-L-homocysteine. It took part in the regulation of body weight and insulin sensitivity. It was reported that NNMT takes a role in various diseases, metabolic disorders, obesity and type 2 diabetes. Additionally, increased expression of NNMT enhances cell proliferation and disease progression in a wide variety of cancers. In the literature, it was suggested that NNMT inhibitors can be developed as drug candidates to treat abovementioned metabolic diseases. [39] Results of molecular docking and MD simulations showed that synthesized compounds can effectively interact with selected target receptors and can be promising structures for further studies.

In computational studies, geometry optimizations, frequency analyses, frontier molecular orbital calculations, molecular electrostatic potential map calculations, IR and NMR spectral analyses were performed.

Considering that the synthesized compounds will have potential pharmaceutical properties based on previous studies in the literature, molecular docking calculations were also performed to estimate the binding affinities of the investigated compounds for NNMT, AChE, HSP90α and SARS-CoV-2 M^{pro}.

In addition to molecular docking calculations, MD simulations were also performed on the ligand-receptor complexes which has the highest scores in molecular docking studies to evaluate the flexibility and stability of the ligand-receptor interactions at the atomic level.

2. Experimental

2.1. Materials and methods

Chemicals used for the synthesis were supplied from Merck and Aldrich Chemical Company without further purification. Solid state IR spectra were noted using a Shimadzu IRAffinity-1 Fourier Transform Infrared (FT-IR) spectrophotometer. Nuclear magnetic resonance (^{1}H NMR) spectra were detected on Agilent 400/54 400 MHz NMR in deuterated dimethyl sulfoxide (DMSO–d6) using tetramethyl silane (TMS) as the internal reference. Chemical shifts (δ) were given in ppm. Melting points were recorded on Thermo Fisher Scientific IA9100 melting point apparatus. Elemental analysis was done on Leco CHNS-932 analyzer.

Computational studies on the synthesized compounds were carried out using Gaussian Rev.D01 software package [40]. Conformational search for each compound was performed with the use of VeraChem Vconf software package [41]. GaussView 5 [42] and Discovery Studio Visualizer [43] software packages were used for the visualization of the results.

In molecular docking calculations AutoDock Tools [44] and AutoDock Vina [45] software packages were used, and Discovery Studio Visualizer [46] was used to visualize the results. The structures of the proteins were obtained from RCSB protein data bank (PDB IDs: 2iip, 1eve, 3qdd, 6lu7) [31,46–48]. The structures of sinefungin, donepezil, ganetespib, remdesivir, hydroxychloroquine and favipiravir were obtained from PubChem Database [49], and the structures of ritonavir and lopinavir were obtained from Zinc Database [50]. Prior to docking calculations, water molecules were removed, polar hydrogens and Gasteiger charges were added and docking calculations were performed with the use of Lamarckian genetic algorithm. Molecular docking calculations were performed in a grid box covering the active sites of AChE, HSP90α and NNMT. In molecular docking calculations performed for SARS-CoV-2 M^{pro}, AutoGridFR software [51] was used for the determination of the binding pocket. Inverse docking calculations were performed with the use of ACID web server [52]. In drug-likeness analyses DruLiTo software package [53] was used. The highest scoring ligand-protein complexes in molecular docking calculations were used in MD simulations for evaluating the stability and the flexibility of ligand-protein interactions at the atomic level. MD simulations were performed with the use of GROMACS [54]. Topology of the proteins were prepared with the use of CHARMM36 forcefield [55] and TIP3P water model. Ligand topologies were obtained from SwissParam server [56]. MD simulations were performed in a dodecahedron box after neutralization. The energy minimizations were carried out by employing steepest descent minimization algorithm. NVT and NPT equilibrations were proceeded in 100 ps, then MD

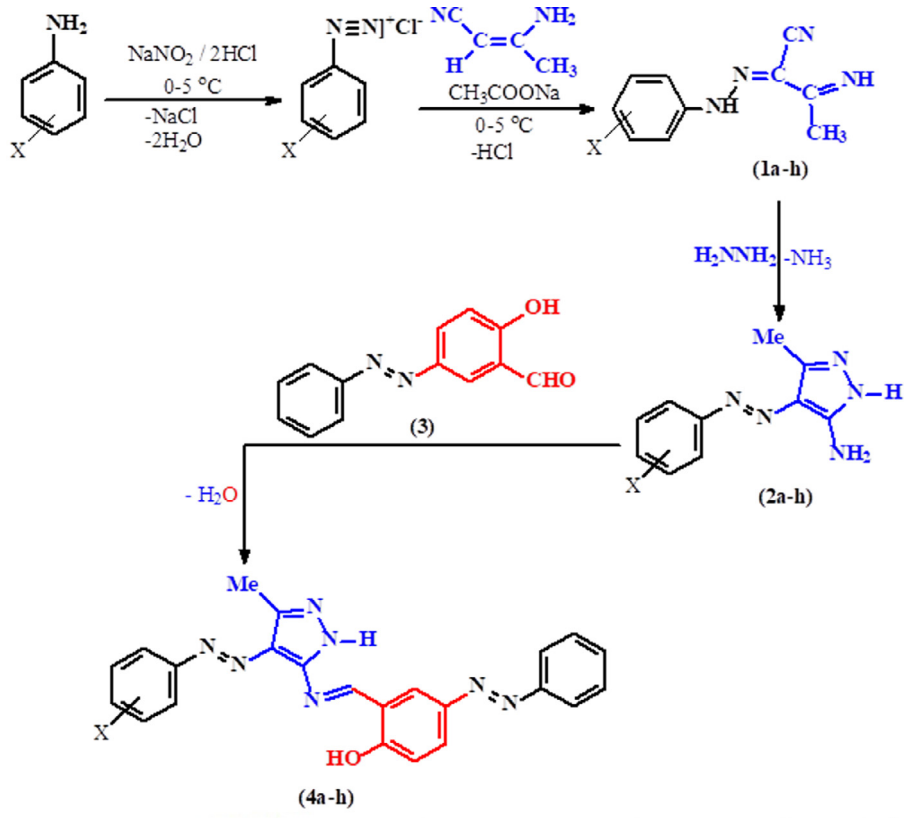

	a	b	c	d	e	f	g	h
X	H	4-OMe	4-Cl	3-NO_2	3-OMe	3-Cl	3-Me	2-OMe

Fig. 1. General route for the synthesis of disazo-azomethine dyes (**4a-**4h).

simulations were performed at 1 bar and 300 K reference pressure and temperature for 30 ns.

2.2. Synthesis

2-Arylhydrazone-3-ketiminobutyronitriles **(1a–**1h**)**, 5-amino-4-arylazo-3-methyl-1*H*-pyrazoles **(2a–**2h**)** and 2–hydroxy-4-(phenyldiazenyl)benzaldehyde **(3)** were prepared according to the literature [57–59]. By using these reagents 2-{[(3-*methyl*-4-((4-*arylphenyl*)*diazenyl*)−1*H*-*pyrazole*-5-*yl*))*imino*]methyl}−5-(phenyldiazenil)phenol compounds **(4a-**4h**)** were synthesized by following method.

2.2.1. General procedure for the synthesis of 2-{[(3-methyl-4-((4-arylphenyl)diazenyl)−1*H*-pyrazole-5-yl))imino*]methyl*}−5-(phenyldiazenil)phenol (4a-4h) compounds

2.01 g (10 mmol) of 3-methyl-4-(phenyldiazenyl)−1*H*-pyrazol-5-amine **(2a)**; was dissolved in 30 ml toluene and poured into 2,26 g (10 mmol) of 2–hydroxy-4-(phenyldiazenyl)benzaldehyde **(3)** - 30 ml toluene mixture in a 250 ml round bottom flask. A Dean-Stark apparatus is placed between flask and condenser for removing the water formed as a result of the reaction, and the mixture is refluxed for 24 h. After the reaction was completed, the yellowish-brown final product was filtered, dried and crystallized by using DMF & water. All **4a-**4h products were synthesized as the method mentioned above, the general route for the synthesis of disazo-azomethine dyes is shown in Fig. 1 and all 2D structures of the synthesized compounds are given in Supplementary Information.

*2.2.1.1. 2-{[3-*methyl-*4*-phenyldiazenyl-*1*H-pyrazole-*5*-yl-imino*]methyl*}−*5-(phenyldiazenil) phenol,* ***4a***. Yellowish-brown crystals, yield 63%, mp 236–237 °C (DMF-H_2O), IR: ν (cm^{-1}) = 1630, ν = 1608 (2 C=N), ν = 1415 (N=N), ν = 3078 (Ar-H), ν = 2977 (CH_3), ^{1}H NMR (DMSO–d_6, 400 MHz) δ = 2.61 (3H, s, CH_3), δ = 7.15 - 8.36 (13H, m, Ar-H), δ = 9.49 (1H, s, N=CH), δ = 13.38 (1H, b, NH), δ = 14.45 (1H, b, OH). Anal Calcd. for $C_{23}H_{19}N_7O$: C, 67.47; H, 4.68; N, 23.95%. Found: C, 67.61; H, 4.59; N, 23.78%.

*2.2.1.2. 2-{[(3-*methyl-*4-((4-*methoxyphenyl)diazenyl)−*1*H-pyrazole-*5*-yl))imino*]methyl*}−*5-(phenyldiazenil) phenol,* ***4b***. Red crystals, yield 72%, mp 236–237 °C (DMF-H_2O), IR: ν (cm^{-1}) = 1649, 1605 (2 C=N), ν = 1423 (N=N), ν = 1242 (C-O-Ar), ν = 3072 (Ar-H), ν = 2968 (CH_3), ^{1}H NMR (DMSO–d_6, 400 MHz) δ = 2.58 (3H, s, CH_3), δ = 3.85 (3H, s, 4–OCH_3), δ = 7.11 - 8.33 (12H, m, Ar-H), δ = 9.46 (1H, s, N=CH), δ = 13.28 (1H, b, NH), δ = 14.54 (1H, b, OH). Anal Calcd. for $C_{24}H_{21}N_7O_2$: C, 65.59; H, 4.82; N, 22.31%. Found: C, 65.44; H, 4.88; N, 22.52%.

*2.2.1.3. 2-{[(3-*methyl-*4-((4-*chlorophenyl)diazenyl)−*1*H-pyrazole-*5*-yl))imino*]methyl*}−*5-(phenyldiazenil) phenol,* ***4c***. Dark red crystals, yield 86%, mp 264.2–264.5 °C (DMF-H_2O), IR ν (cm^{-1}) = 1635, 1606 (2 C=N), ν = 1421 (N=N), ν = 3066 (Ar-H), ν = 2936 (CH_3), ^{1}H NMR (DMSO–d_6, 400 MHz) δ = 2.59 (3H, s, CH_3), δ = 7.13 - 8.33 (12H, m, Ar-H), δ = 9.46 (1H, s, N=CH), δ = 13.41 (1H, b, NH), δ = 14.43 (1H, b, OH). Anal Calcd. for $C_{23}H_{18}ClN_7O$: C, 62.23; H, 4.09; N, 22.09%. Found: C, 62.36; H, 4.20; N, 22.27%.

*2.2.1.4. 2-{[(3-*methyl-*4-((3-*nitrophenyl)diazenyl)−*1*H-pyrazole-*5*-yl))imino*]methyl*}−*5-(phenyldiazenil) phenol,* ***4d***. Red crystals, yield

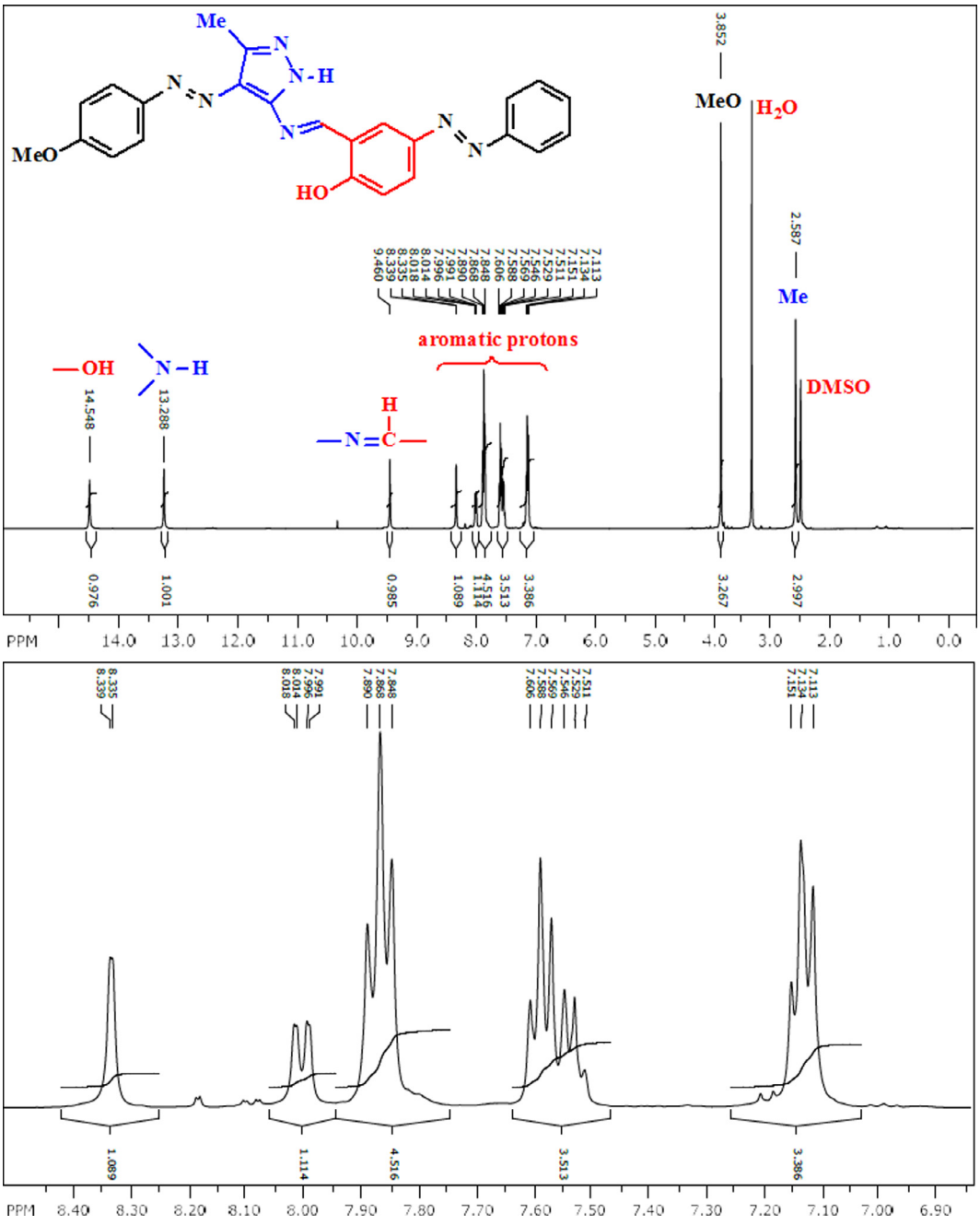

Fig. 2. ^{1}H NMR spectrum of **4b** in DMSO–d_6.

63%, mp 266–267 °C (DMF-H_2O), IR: ν (cm^{-1}) = 1630, 1604 (2 C=N), ν = 1415 (N=N), ν = 1523,1350 (N=O), ν = 3095 (CH_3), ν = 2966 (Al-H), ^{1}H NMR (DMSO–d_6, 400 MHz) δ = 2.59 (3H, s, CH_3), δ = 7.09 - 8.50 (12H, m, Ar-H), δ = 9.42 (1H, s, N=CH), δ = 13.46 (1H, b, NH), δ = 14.36 (1H, b, OH). Anal Calcd. for $C_{23}H_{18}N_8O_3$: C, 60.79; H, 3.99; N, 24.66%. Found: C, 60.61; H, 3.92; N, 24.50%.

2.2.1.5. 2-{[(3-methyl-*4-((3*-methoxyphenyl)diazenyl)*–1*H-pyrazole-*5*-yl)*)*imino*]methyl}*–5-(phenyldiazenil) phenol,* ***4e****.* Brownish yellow crystals, yield 75%, mp 215–216 °C (DMF-H_2O), IR: ν (cm^{-1}) = 1630, 1606 (2 C=N), ν = 1429 (N=N), ν = 1240 (C–O-Ar), ν = 3057 (Ar-H), ν = 2960 (CH_3), ^{1}H NMR (DMSO–d_6, 400 MHz) δ = 2.60 (3H, s, CH_3), δ = 3.85 (3H, s, 3–OCH_3), δ = 7.05 - 8.33 (12H, m, Ar-H), δ = 9.47 (1H, s, N=CH), δ = 13.38 (1H, b, NH), δ = 14.43 (1H, b, OH). Anal Calcd. for $C_{24}H_{21}N_7O_2$: C, 65.59; H, 4.82; N, 22.31%. Found: C, 65.67; H, 4.68; N, 22.59%.

2.2.1.6. 2-{[(3-methyl-*4-((3*-chlorophenyl)diazenyl)*–1*H-pyrazole-*5*-yl)*)*imino*]methyl}*–5-(phenyldiazenil) phenol,* ***4f****.* Red crystals, yield 67%, mp 223.4–223.9 °C (DMF-H_2O), IR: ν (cm^{-1}) = 1635, 1606 (2 C=N), ν = 1423 (N=N), ν = 3055 (Ar-H), ν = 2974 (CH_3), ^{1}H NMR (DMSO–d_6, 400 MHz) δ = 2.60 (3H, s, CH_3), δ = 7.12 - 8.31 (12H, m, Ar-H), δ = 9.44 (1H, s, N=CH), δ = 13.42 (1H, b, NH), δ = 14.38 (1H, b, OH). Anal Calcd. for $C_{23}H_{18}ClN_7O$: C, 62.23; H, 4.09; N, 22.09%. Found: C, 62.41; H, 4.00; N, 21.97%.

2.2.1.7. 2-{[(3-methyl-*4-((3*-methylphenyl)diazenyl)*–1*H-pyrazole-*5*-yl)*)*imino*]methyl}*–5-(phenyldiazenil) phenol, 4 g.* Red crystals, yield 57%, mp 230–231 °C (DMF-H_2O), IR: ν (cm^{-1}) = 1635, 1606

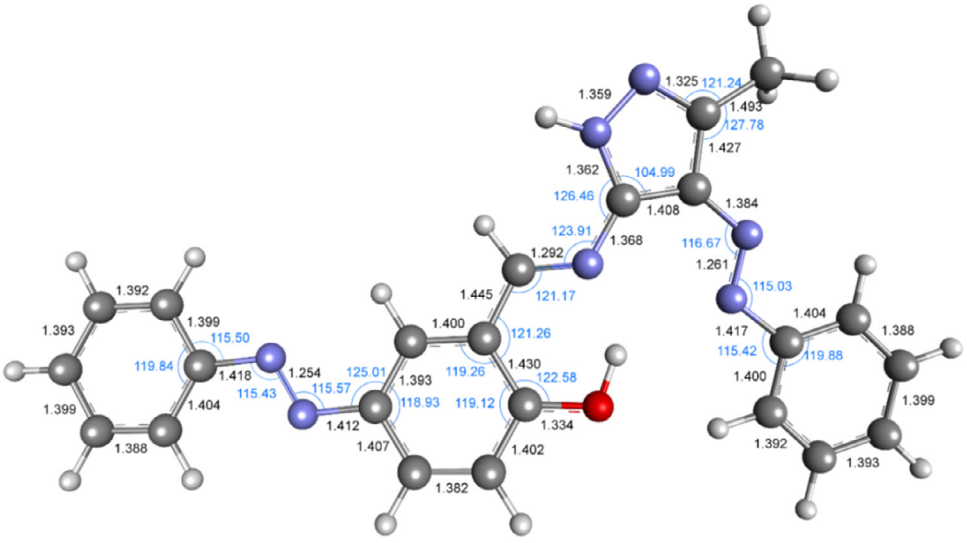

Fig. 3. Optimized geometry and selected geometric parameters of **4a** (bond lengths are in black and bond angles are in blue).

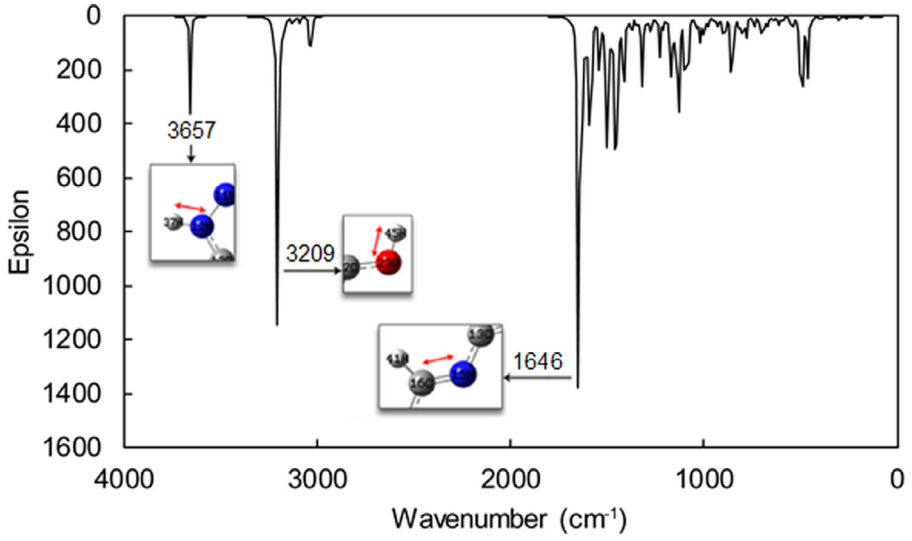

Fig. 4. Calculated vibrational spectra for compound **4d**

Table 1
Selected peaks for investigated compounds.

	N-H stretching (computional) (cm^{-1})	O-H stretching (computional) (cm^{-1})	C=N$_{(azomethine)}$ stretching (computional) (cm^{-1})	C=N$_{(azomethine)}$ stretching (experimental) (cm^{-1})
4a	3657	3217	1647	1630
4b	3661	3195	1646	1649
4c	3658	3207	1647	1635
4d	3657	3209	1646	1630
4e	3658	3200	1647	1630
4f	3657	3216	1647	1635
4g	3654	3199	1645	1635
4h	3656	3258	1639	1664

(2 C=N), ν = 1417 (N=N), ν = 3055 (Ar-H), ν = 2954 (CH_3), ^{1}H NMR (DMSO–d_6, 400 MHz) δ = 2.59 (3H, s, CH_3), δ = 2.36 (3H, s, 3-CH_3), δ = 7.11 - 8.33 (12H, m, Ar-H), δ = 9.47 (1H, s, N=CH), δ = 13.36 (1H, b, NH), δ = 14.35 (1H, b, OH). Anal Calcd. for $C_{24}H_{21}N_7O$: C, 68.07; H, 5.00; N, 23.15%. Found: C, 68.24; H, 4.87; N, 23.29%.

*2.2.1.8. 2-{[(3-*methyl*-4-((2-*methoxyphenyl*)*diazenyl*)–1*H*-pyrazole-5-*yl*))*imino*]methyl}–5-(phenyldiazenil) phenol, 4h.* Dark yellow crystals, yield 54%, mp 204–205 °C (DMF-H_2O), IR: ν (cm^{-1}) = 1664, 1610 (2 C=N), ν = 1414 (N=*N*), ν = 1242 (C-O-Ar), ν = 3066 (Ar-H), ν = 2961 (CH_3), ^{1}H NMR (DMSO–d_6, 400 MHz) δ = 2.57 (3H, s, CH_3), δ = 3.89 (3H, s, 2–OCH_3), δ = 7.09 - 8.38 (12H, m, Ar-H), δ = 9.52 (1H, s, N=CH), δ = 13.31 (1H, b, NH), δ = 13.88 (1H, b, OH). Anal Calcd. for $C_{24}H_{21}N_7O_2$: C, 65.59; H, 4.82; N, 22.31%. Found: C, 65.28; H, 5.01; N, 22.58%.

3. Results and discussion

Synthesized compounds are prepared by using aniline derivatives by diazotization, coupling, ring closing and condensation reactions respectively. All synthesized compounds are characterized by elemental analysis and spectroscopic methods.

Proton	Chemical Shift (ppm)
32-H	8.64
33-H	7.71
34-H	7.61
35-H	7.71
36-H	8.64
37-H	8.96
38-H	2.74
39-H	2.74
40-H	2.74
41-H	9.02
42-H	8.40
43-H	8.38
44-H	7.44
45-H	13.66
46-H	8.36
47-H	7.69
48-H	7.59
49-H	7.69
50-H	8.36

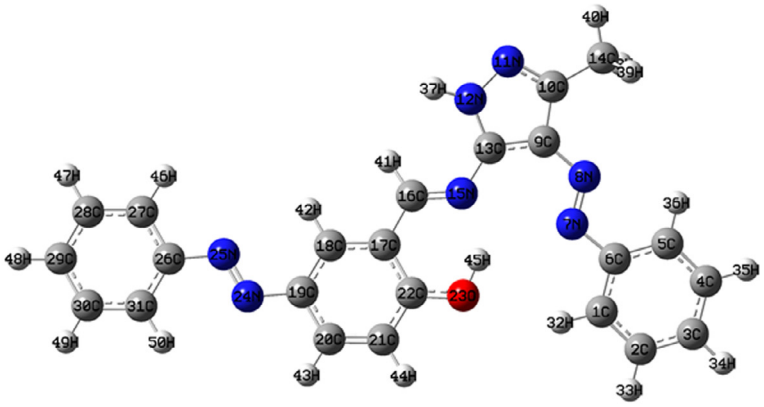

Fig. 5. Structure and calculated ^{1}H NMR chemical shifts for **4a**.

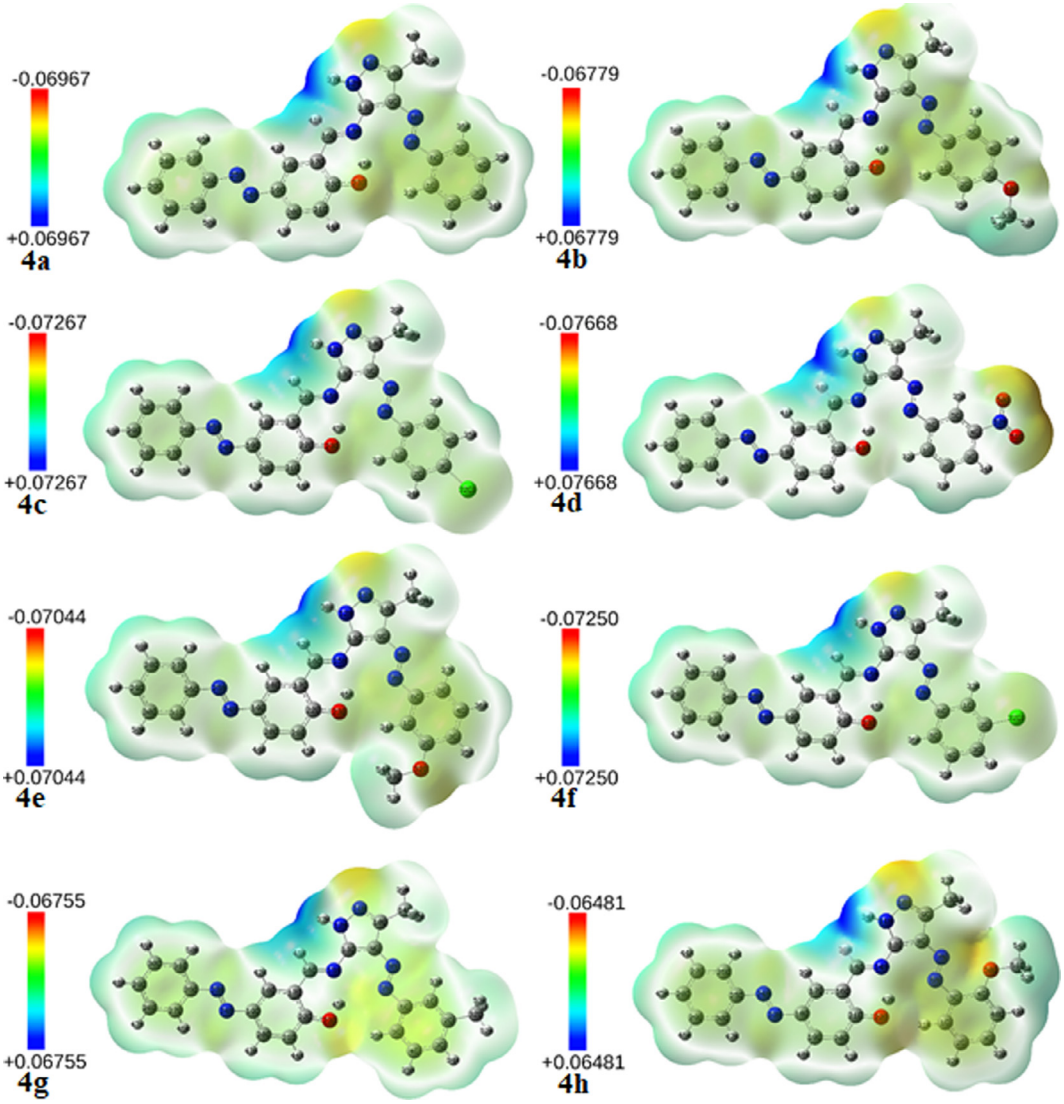

Fig. 6. Molecular electrostatic potential maps of the investigated compounds.

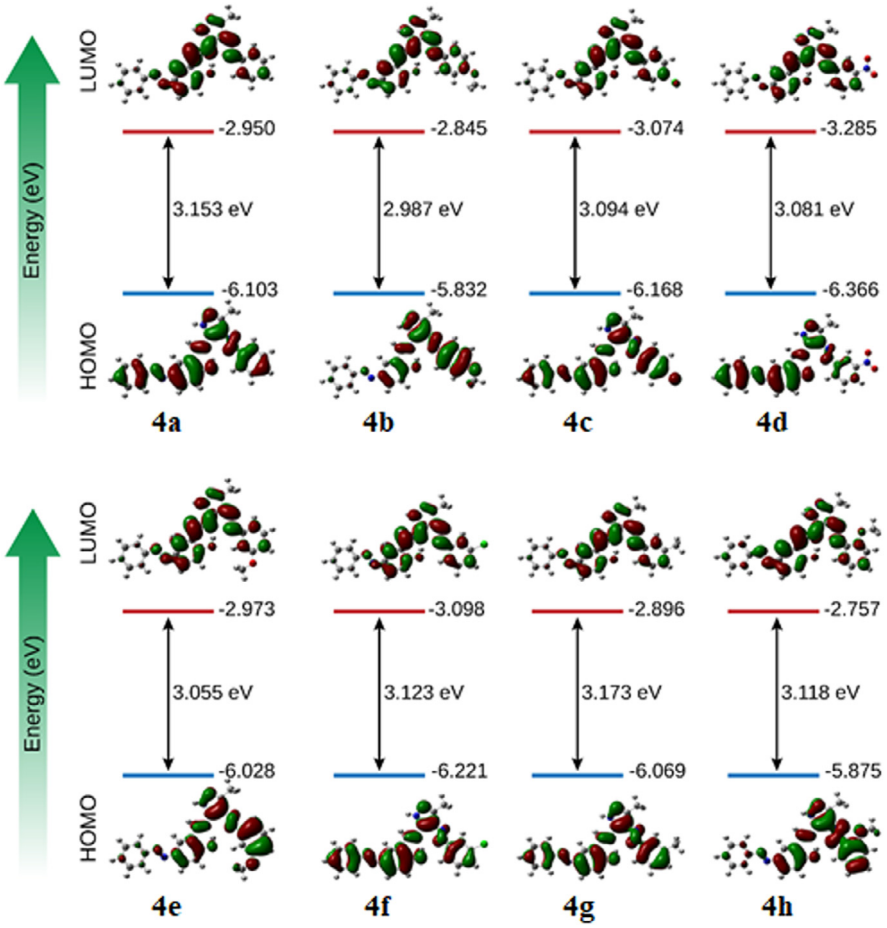

Fig. 7. FMOs and HOMO-LUMO gaps for **4a-**4h.

Table 2
Calculated global reactivity descriptors for **4a-**4h.

	4a	4b	4c	4d	4e	4f	4g	4h
HOMO	−6.10297	−5.83222	−6.16801	−6.36556	−6.02760	−6.22080	−6.06869	−5.87548
LUMO	−2.94972	−2.84468	−3.07407	−3.28469	−2.97285	−3.09829	−2.89556	−2.75706
Gap	3.15326	2.98754	3.09394	3.08087	3.05475	3.12251	3.17312	3.11843
I	6.10297	5.83222	6.16801	6.36556	6.02760	6.22080	6.06869	5.87548
A	2.94972	2.84468	3.07407	3.28469	2.97285	3.09829	2.89556	2.75706
S	0.63426	0.66945	0.64643	0.64917	0.65472	0.64051	0.63029	0.64135
η	1.57663	1.49377	1.54697	1.54044	1.52738	1.56125	1.58656	1.55921
μ	−4.52634	−4.33845	−4.62104	−4.82512	−4.50022	−4.65954	−4.48213	−4.31627
χ	4.52634	4.33845	4.62104	4.82512	4.50022	4.65954	4.48213	4.31627
ω	6.49734	6.30022	6.90189	7.55689	6.62967	6.95318	6.33113	5.97423

3.1. FT-IR results

Examining FT-IR spectra of the **4a-**4h compounds, it was observed that the C=O stretching vibrations of compound **3** at ν = 1668 cm^{-1} disappeared [59]. In addition to that, at synthesized **2a-**2h compounds, the doublets of the primary N-H stretching observed [57,58,60] in the 3400–3456 and 3292–3362 cm^{-1} regions disappeared, instead, large absorptions of O-H and N-H stretching in the 3100–3400 cm^{-1} region appeared.

In **4a-**4h compounds there are two types of C=N stretching vibrations, which are azomethine C=N and imidazole C=N. FT-IR spectra showed that azomethine and imidazole C=N stretching vibrations were found to be in 1630–1664 cm^{-1} and 1604–1610 cm^{-1} regions, respectively.

In some compounds azomethine C=N and imidazole C=N stretching vibrations were seen separately, while in others this distinction was not clearly observed. O-H, N-H, C=N, N=N (1414–1429 cm^{-1}) and N=O (**4d**: 1523, 1350 cm^{-1}) absorptions are compatible with the literature [12,59,61].

3.2. ^{1}H NMR spectra

^{1}H NMR spectrum of compound **4b** is given in Fig. 2 and inspections were made through this compound. When the previous studies in the literature were examined[59, 60], amino group peaks on the pyrazole ring of **2a-**2h compounds, which were observed between 6.40–6.70 ppm, and the aldehyde peak of compound **3**, observed at 10.36 ppm, both disappeared. It is seen that instead

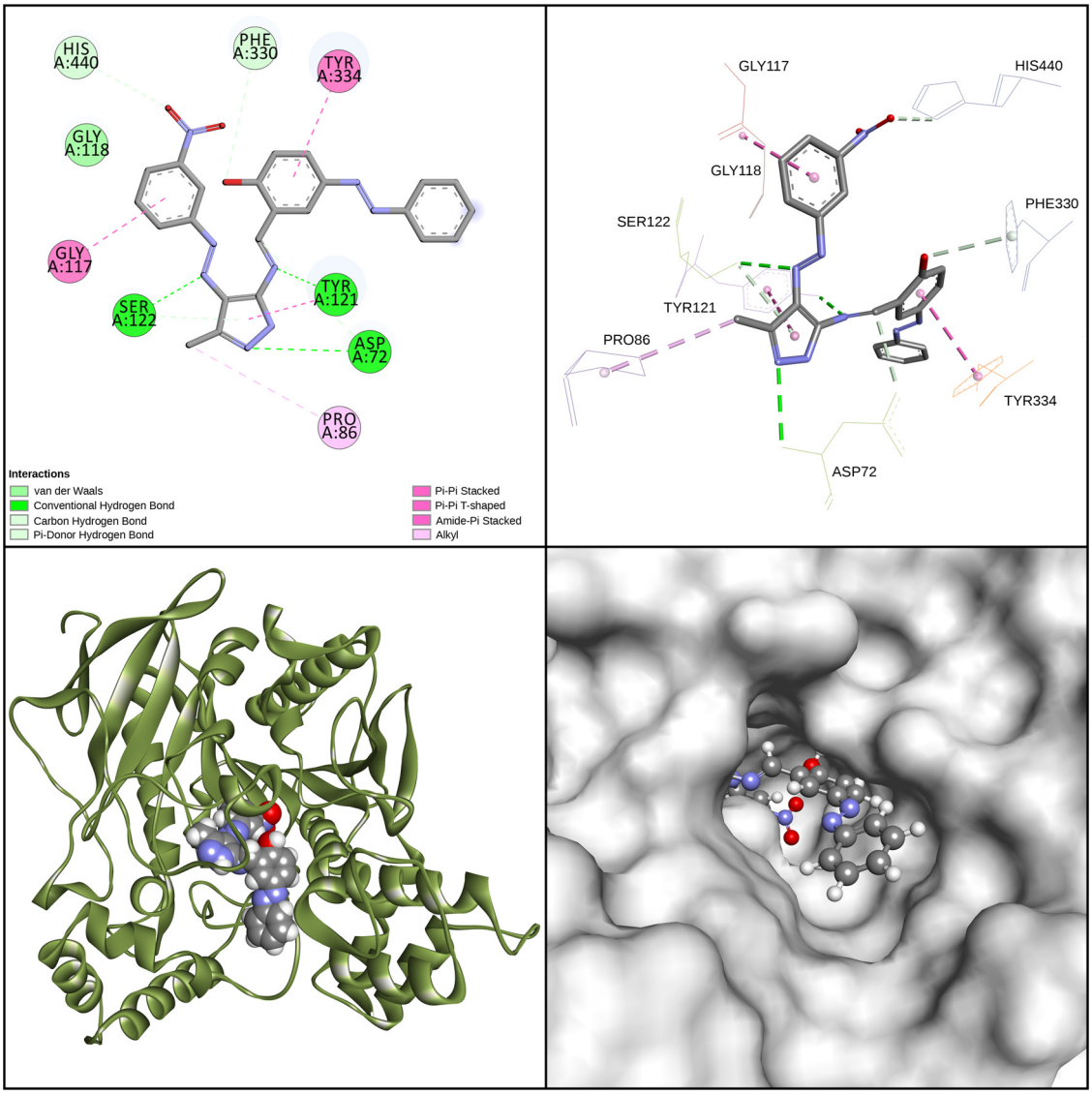

Fig. 8. Representation of the molecular docking results for 4d – AChE complex.

Table 3
Calculated binding affinities of **4a-**4h and reference molecules.

Compound	Binding Scores (kcal/mol)			
	NNMT (2iip)	**AChE (1eve)**	**HSP90α (3qdd)**	**SARS-CoV-2 M^{pro} (6lu7)**
4a	−11.8	−11.0	−11.3	−8.2
4b	−11.6	−10.1	−10.1	−8.0
4c	−11.8	−10.8	−11.4	−8.0
4d	−11.5	−11.6	−11.2	−8.7
4e	−12.2	−11.4	−11.1	−8.0
4f	−12.0	−11.3	−11.2	−8.4
4g	−12.3	−11.1	−11.0	−8.6
4h	−10.6	−10.8	−10.8	−8.0
Sinefungin	−9.0	–	–	–
Donepezil	–	−10.7	–	–
Ganetespib	–	–	−10.2	–
Remdesivir	–	–	–	−8.2
Ritonavir	–	–	–	−7.0
Lopinavir	–	–	–	−6.8
Hydroxychloroquine	–	–	–	−6.2
Favipiravir	–	–	–	−5.0

of these two peaks, an azomethine peak formed between 9.42–9.52 ppm in **4a-**4h compounds. As a result of the desired Schiff base formation on compound **4e**, the δ = 12.10 ppm peak of the -NH proton in the pyrazole ring and the δ = 11.52 ppm peak of the -OH proton in the salicylidene ring slightly slided down to δ = 13.28 ppm and δ = 14.54 ppm, respectively.

It has been recorded that the protons attached to the aromatic ring had multiplets at δ = 7.05–8.50. The protons in the methoxy group attached to the aromatic ring had singlets at δ = 3.85, 3.85 and 3.89 ppm on *para-*, *meta-* and *ortho-* positions respectively. The protons in the methyl group attached to the pyrazole ring had singlets between δ = 2.57–2.61 ppm, while methyl protons attached to the aromatic ring at *ortho-* position had multiplets at δ = 2.36.

3.3. Computational studies

In computational studies, geometry optimizations, frequency analyses, frontier molecular orbital calculations, molecular electrostatic potential map calculations, FT-IR and NMR spectral analyses were performed. Molecular docking calculations and MD simulations were also performed to estimate the binding affinities of the

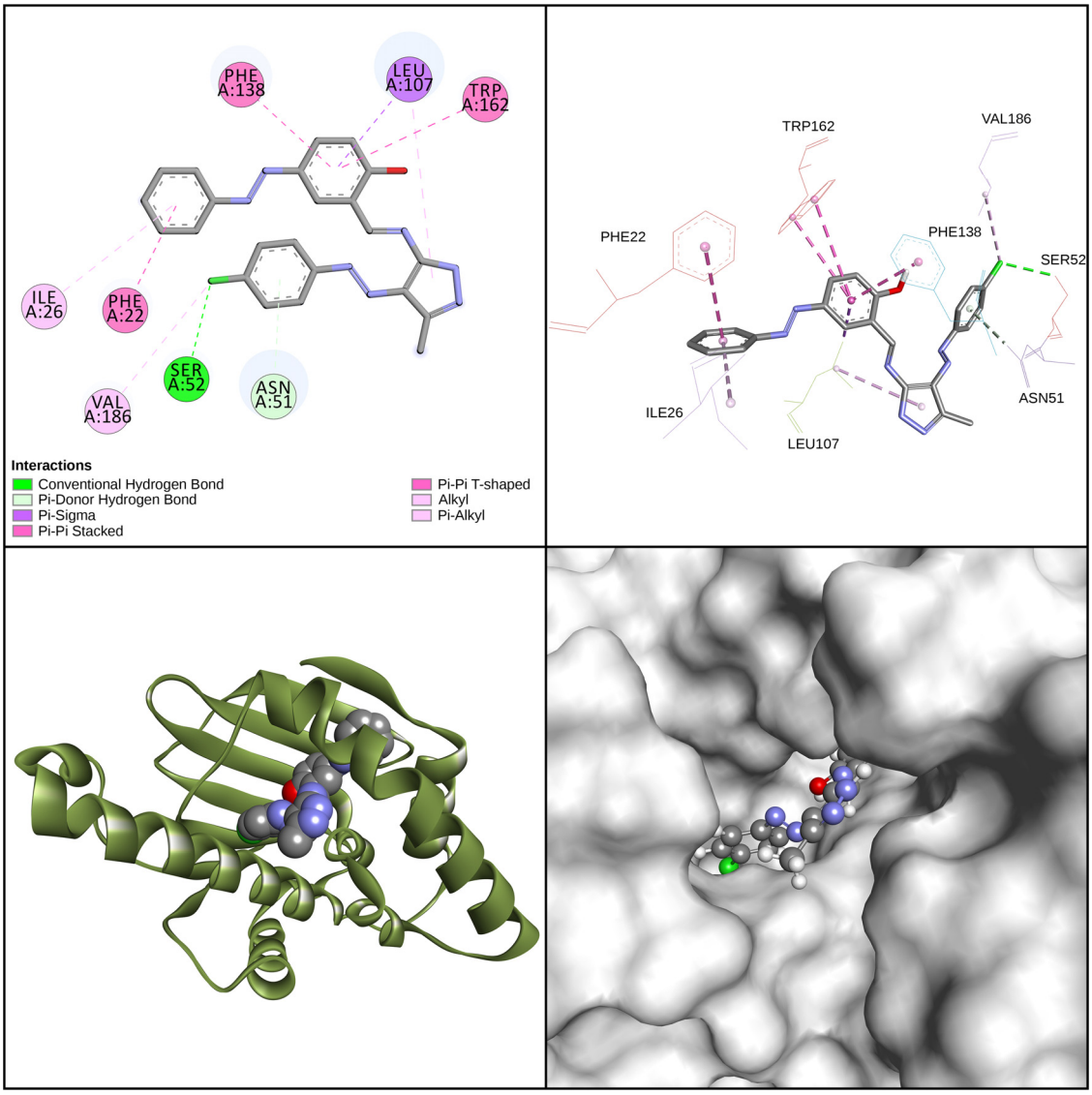

Fig. 9. Representation of the molecular docking results for 4c – HSP90α complex.

investigated compounds for selected proteins, and to investigate the interactions between synthesized compounds and target receptors.

3.3.1. Geometry optimizations

Geometry optimizations were performed by DFT approach with the use of B3LYP (Becke-3-Lee-Yang-Parr) functional and 6–311+*G*(d,p) basis set. To confirm that each optimized geometry corresponds to a global minimum, frequency analyses were also performed on the investigated compounds. Optimized geometries of the investigated compounds are given in Supplementary Information. Fig. 3 shows, as an example, optimized geometry and some geometric parameters for compound **4a**.

3.3.2. Vibrational spectra and frequency analyses

Vibrational spectra of the compounds were obtained from the frequency analyses which were performed with the use of DFT/B3LYP method and 6–311+*G*(d,p) basis set. Calculations were performed in gas phase and no scaling factors were applied. Vibrational spectra of the investigated compounds are given in Supplementary Information. As an example, spectra of compound **4d** is given in Fig. 4.

In Fig. 4, peaks which correspond to N-H stretching, O-H stretching and C=N stretching were observed at 3657, 3209 and 1646 cm^{-1}, respectively. Same peaks for all **4a-h** compounds are shown in Table 1. There are no significant difference on investigated compounds for C=N stretching. Computational studies of **4a-**4h compounds were unable to be compared with the experimental data due to N-H and O-H stretching vibrations' overlapping on experimental spectra. Table 1 includes both computational and experimental azomethine C=N stretching vibration values.

3.3.3. NMR spectral analyses

In the study, NMR spectral analyses were also carried out at DFT level with the use of with the use of DFT/B3LYP method and 6–311+*G*(d,p) basis set. In these calculations GIAO (Gauge Independent Atomic Orbital) method was used. Results for all **4a-**4h compounds are given in Supplementary Information section and the result of compound **4a** is given in Fig. 5 as an example.

3.3.4. Molecular electrostatic potential map calculations

Molecular electrostatic potential (MEP) maps of the investigated compounds, which gives information about electron deficient and rich parts of a molecule, were obtained at the same level of theory.

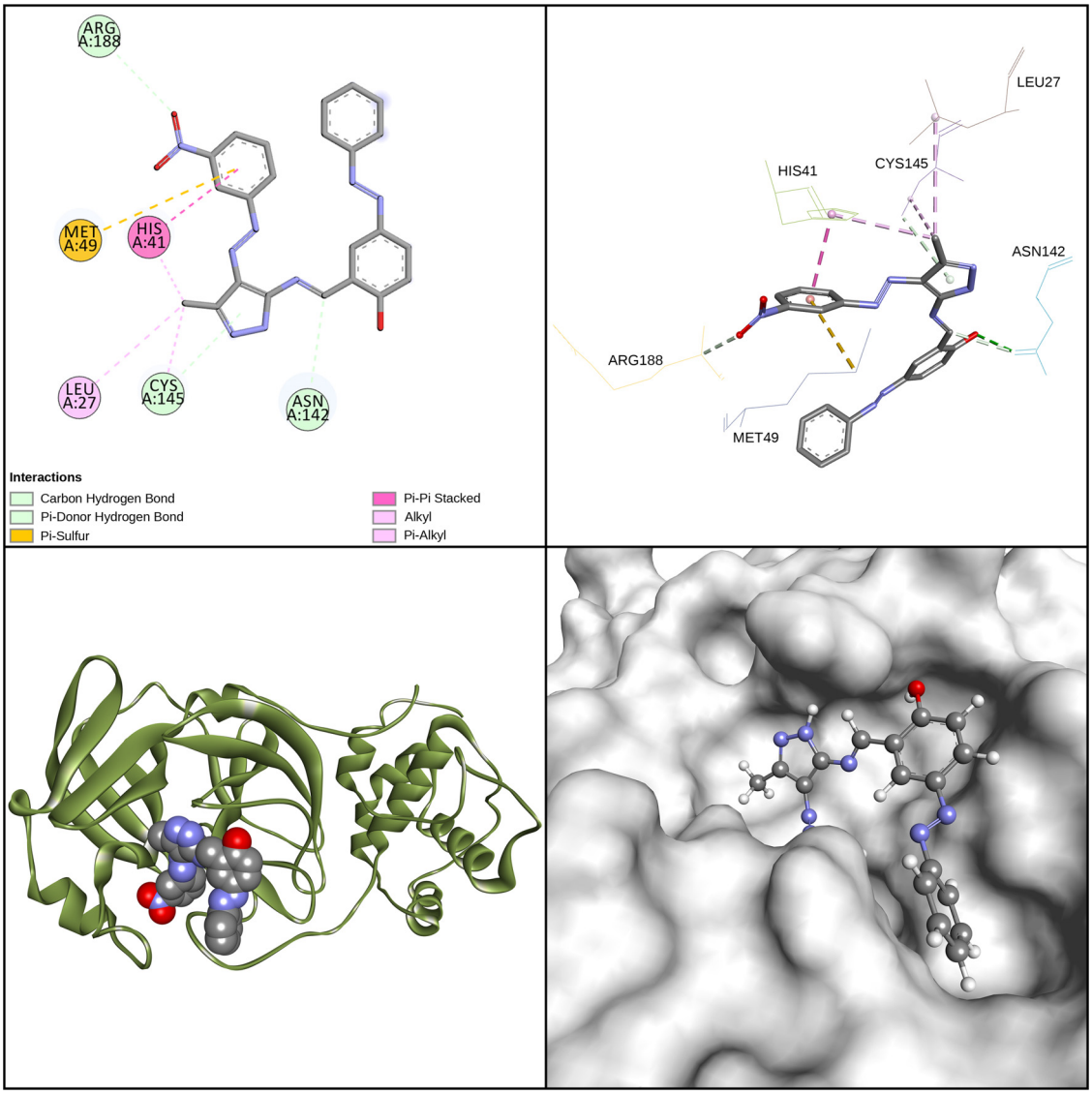

Fig. 10. Representation of the molecular docking results for 4d – SARS-CoV-2 M^{pro} complex.

Calculated MEP maps of the investigated compounds are given in Fig. 6 and also in Supplementary Information. For all compounds, negative charge was localized on the oxygen atom(s), aromatic rings, chlorine atom (if present), and on the nitrogen atoms other than N-H group while positive charge was localized dominantly on hydrogen atom of the N-H group. In molecular docking and MD simulations studies, it was observed that these positive and negative regions took part in the interactions between ligand and receptors.

3.3.5. Frontier molecular orbitals and global reactivity descriptors

The frontier molecular orbitals (FMOs) participate in chemical reactivity. HOMO-LUMO gap determines the chemical stability of a molecule. In the study, FMOs were computed at the same level of theory. FMOs and HOMO-LUMO gaps of the investigated compounds are given in Fig. 7. HOMO-LUMO gaps order is as follows: 4 g > **4a** > **4f** > 4h > **4c** > **4d** > **4e** > **4b**. As a result it can be said the most stable compound is 4 g.

In this part, some global reactivity descriptors such as ionization potential (I), electron affinity (A), electronic chemical potential ($_{o}$), electrophilicity index (ω), electronegativity (χ) chemical softness (S) and chemical hardness (η) were calculated for **4a-**4h with the use of Eqs. (1)–(7) [62–69] and are given in Table 2.

$$I = - - E_{HOMO} \quad (1)$$

$$A = - - E_{LUMO} \quad (2)$$

$$\chi = (I + A)/2 \quad (3)$$

$$\eta = (I - -A)/2 \quad (4)$$

$$S = 1/\eta \quad (5)$$

$$\mu = - - (I + A)/2 \quad (6)$$

$$\omega = \mu^2/2\eta \quad (7)$$

Ionization potential (I) is described as the amount of energy required to remove an electron from an isolated atom or molecule while electron affinity (A) is described as the amount of energy liberated when an electron is added to an atom or molecule. In the

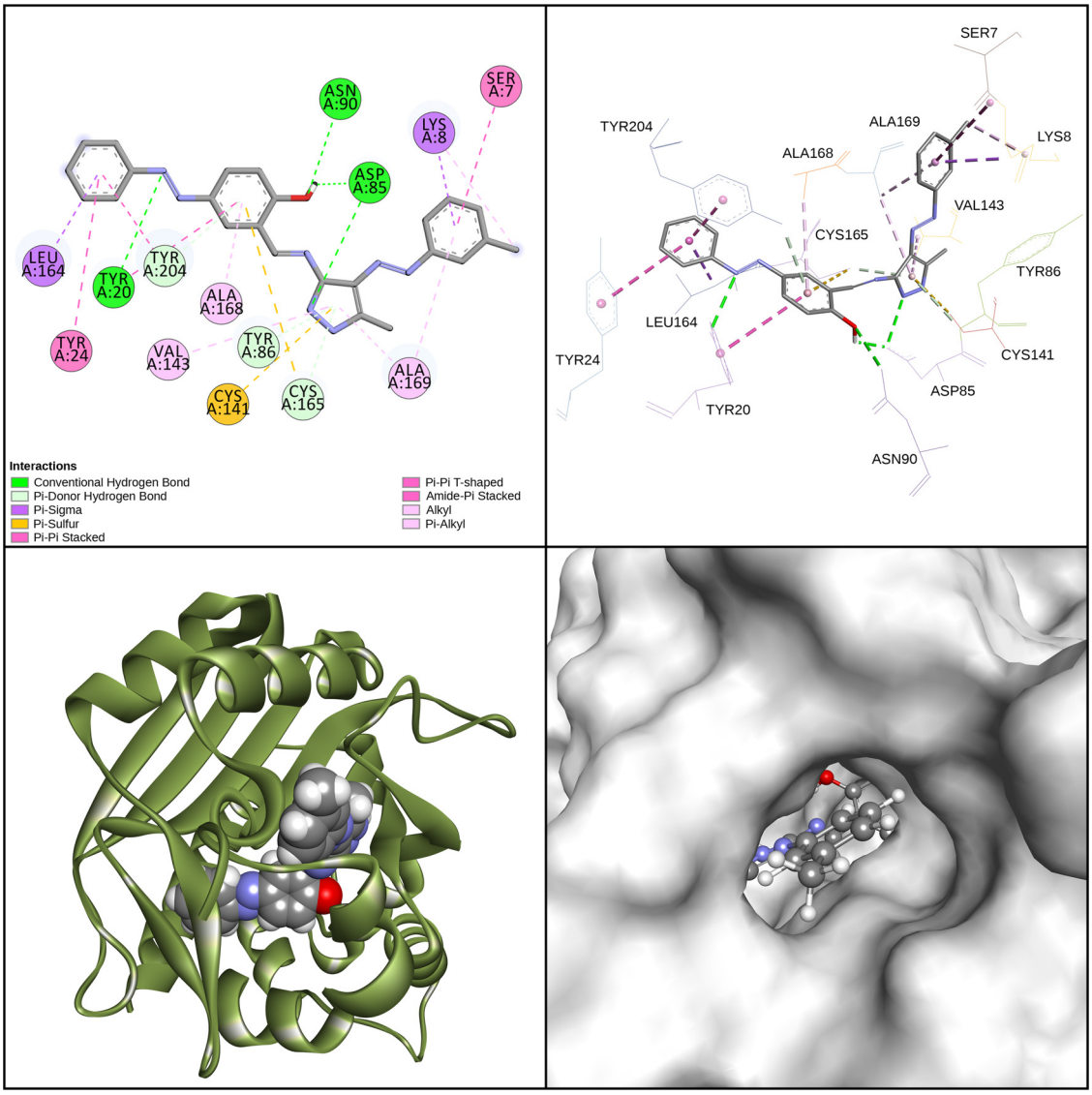

Fig. 11. Representation of the molecular docking results for 4g – NNMT complex.

study, the highest ionization potential was estimated for **4d** while the lowest value obtained for **4b**. Chemical hardness (η) is a measure of resistance of a molecular system to change of its electron distribution and shows a similar trend to the HOMO-LUMO gaps. In the study the highest chemical hardness was obtained for 4 g. Chemical softness (S) is the inverse of chemical hardness and in the study, the lowest chemical softness was obtained for 4 g. Electronic chemical potential (μ) is a measure of escaping tendency of electrons from a system.

In the study, the lowest value of electronic chemical potential was obtained for **4d** Electronegativity (χ) is the negative of the electronic chemical potential, thus, in the study highest electronegativity was obtained for **4d** Since, low electronic chemical potential and high electronegativity correspond to a better electrophilic character, the highest electrophilicity index (ω) was obtained for **4d**, as expected.

3.3.6. Molecular docking calculations

Molecular docking calculations were performed for selected proteins (NNMT, AChE, HSP90α and SARS-CoV-2 M^{pro} to estimate that how synthesized compounds bind to the active site of these selected proteins. Results of inverse docking calculations showed that the synthesized compounds interacted effectively with NNMT. Since the increased expression of NNMT causes disease progression in a wide variety of cancers and various diseases, and inhibitors of this enzyme is suggested as drug candidates, the NNMT inhibition potential of the synthesized compounds were investigated via molecular docking and MD simulations.

As it is well known, AChE inhibitors are used to treat some central nervous system diseases such as Alzheimer's disease, while

Table 4
Calculated binding selectivities of **4a-**4h.

	Binding Selectivities					
Compounds	**2iip:1eve**	**2iip:3qdd**	**2iip:6lu7**	**1eve:3qdd**	**1eve:6lu7**	**3qdd:6lu7**
4a	3.9	2.3	431.9	0.6	112.1	186.0
4b	12.5	12.5	431.9	1.0	34.5	34.5
4c	5.4	2.0	605.1	0.4	112.1	308.3
4d	0.8	1.7	112.1	2.0	132.7	67.6
4e	3.9	6.4	1187.6	1.7	308.3	186.0
4f	3.3	3.9	431.9	1.2	132.7	112.1
4g	7.6	8.9	511.3	1.2	67.6	57.1
4h	0.7	0.7	80.1	1.0	112.1	112.1

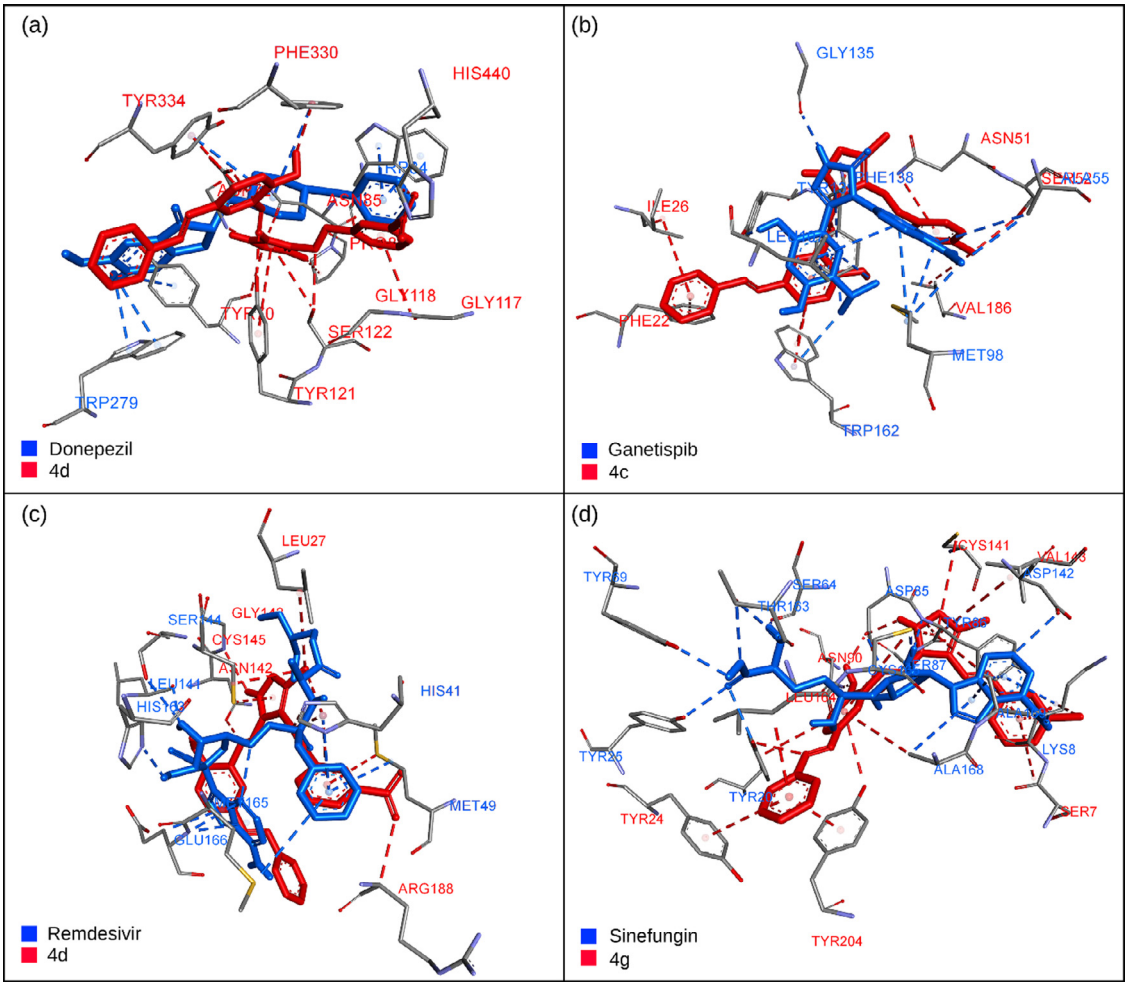

Fig. 12. Comparisons of top-scoring synthesized compounds and reference molecules (a) Donepezil – AChE and 4d – AChE complexes, (b) Ganetispib – HSP90α and 4c – HSP90α complexes, (c) Remdesivir – SARS-CoV-2 M^{pro} and 4d – SARS-CoV-2 M^{pro} complexes and (d) Sinefungin – NNMT and 4g – NNMT complexes.

Table 5
Drug-likeness analyses results.

Parameter	criteria	Calculated value							
		4a	**4b**	**4c**	**4d**	**4e**	**4f**	**4g**	**4h**
MW*	< 500	409.17	439.18	443.13	454.15	439.18	443.13	423.18	439.18
logP**	< 5	4.676	4.705	5.042	4.682	4.705	5.042	5.068	4.705
HBD***	< 5	2	2	2	2	2	2	2	2
HBA****	< 10	8	9	8	8	9	8	8	9

*Molecular Weight; **octanol-water partition coefficient; ***H-Bond Donor; ****H-Bond Acceptor.

heat shock protein inhibitors can be used for the treatment of various types of malignancies.

Many studies have been reported on acetylcholinesterase inhibition. One of the most important and effective AChE inhibitors in the market, which is marketed under the trade name Aricept, is donepezil. Therefore, donepezil was selected as a reference molecule for molecular docking calculations in this study.

Ganetespib is also selected as reference molecule because of being an important HSP90α inhibitor with potential antineoplastic activity. HSP90α takes part in protein folding and in the stabilization of proteins; it has important role in the stabilization of a number of proteins required for tumor growth hence it was also widely accepted that inhibition of this protein could contribute to the treatment of different kinds of cancer.

On the other hand, the epidemic caused by the SARS-CoV-2 continues to cause many people to die all over the world. Although the studies on this issue are gaining speed, the studies are gathered in three groups as (1) vaccine development, (2) the use of existing drugs against the new type of virus and (3) new drug design. Some recent studies involve the inhibition of SARS-CoV-2 M^{pro} [70–80], so in this study we intended to test the activity of newly synthesized compounds against SARS-CoV-2 M^{pro} via molecular docking calculations.

In this part, in addition to newly synthesized compounds, binding affinities of some known inhibitors were also estimated. Calculated binding affinities of the compounds are shown in Table 3.

Binding affinities of the investigated compounds for AChE were found to be in the range of −10.1–−11.6 kcal/mol. It was found that almost all compounds show identical or higher binding affinity according to donepezil.

In the study, it was found that the binding affinities of the investigated compounds for HSP90α are in the range of −10.1 to

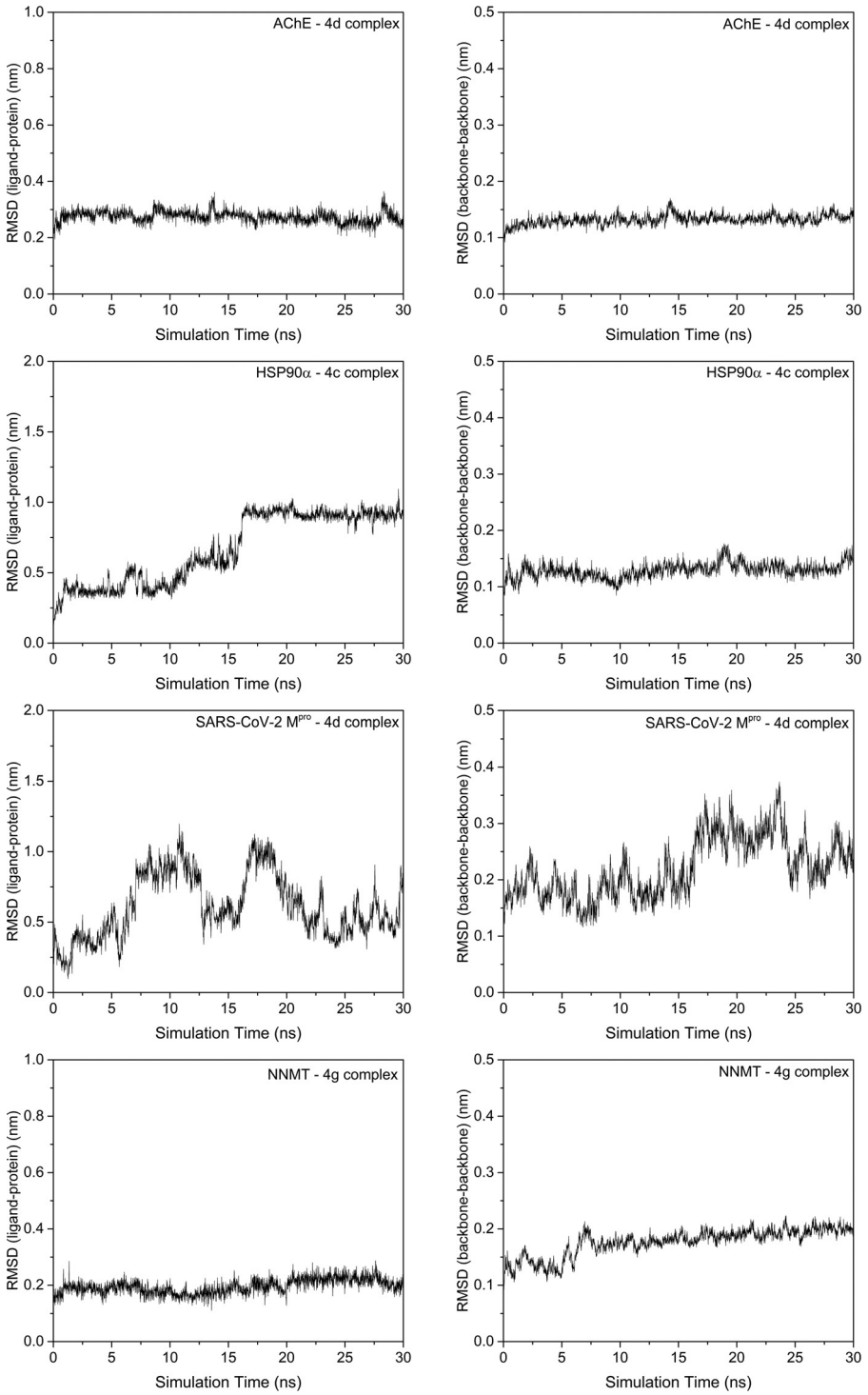

Fig. 13. RMSDs of ligands after least square fit to proteins and RMSDs of proteins after least square fit to proteins.

−11.4 kcal/mol while the binding affinity of the reference molecule ganetespib is −10.2. These results show that almost all the synthesized compounds possess higher binding affinity than ganetespib. The highest binding affinity was observed for 4c. Molecular docking results showed that in HSP90α – 4c complex, chlorine atom at the para- position

Lastly the binding affinities of the investigated compounds for SARS-CoV-2 M^{pro} were found to be in the range of −8.0–−8.7 kcal/mol. To make a comparison, binding affinities of some selected reference molecules (remdesivir, ritonavir, lopinavir, hydroxychloroquine and favipiravir) which are recommended compounds for the treatment of COVID-19 were calculated also.

Results show that newly synthesized compounds show almost identical binding affinity with remdesivir. On the other hand, it was found that the calculated binding affinities of the investigated compounds are higher than those of ritonavir, lopinavir, hydroxychloroquine and favipiravir.

These results show that investigated compounds possess good binding affinity for AChE, HSP90α, SARS-CoV-2 M^{pro} and NNMT. Thus, it can be concluded that the newly synthesized compounds

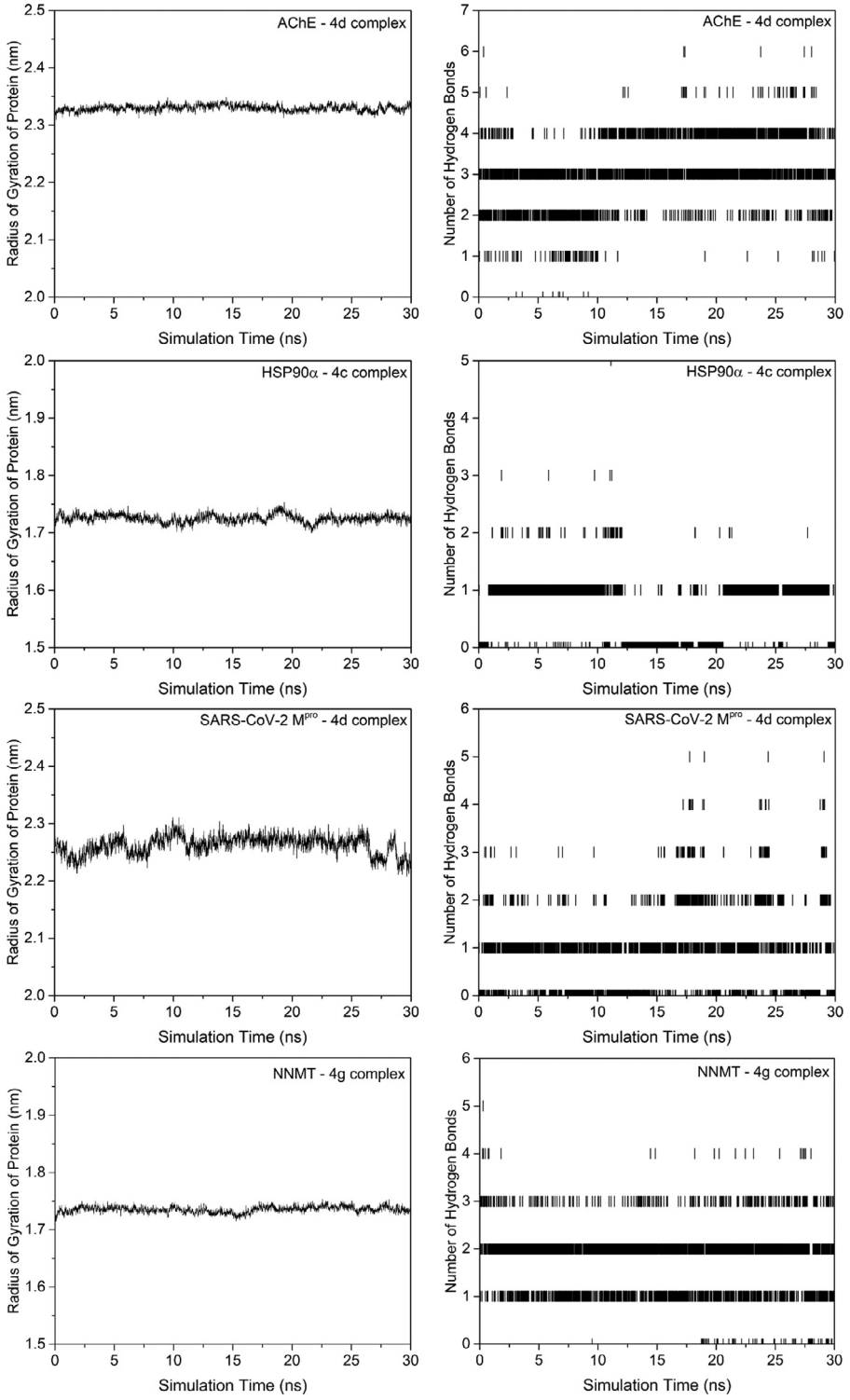

Fig. 14. Radius of gyrations of proteins and number of hydrogen bonds formed between ligands and receptors during the MD simulations.

can be promising structures as potential inhibitors for AChE, HSP90α, SARS-CoV-2 and NNMT. For AChE and SARS-CoV-2 M^{pro}, the highest binding affinity values were obtained for **4d,** and for HSP90α and NNMT, the highest binding affinity values were obtained for **4c** and 4 g, respectively. Results showed that **4d** interacted with TYR334, PHE330, ASP72, TYR121, ASN85, TYR70, PRO86, SER122, GLY118, GLY117 and HIS440 amino acids of AChE. In AChE–4d complex, an additional hydrogen bond was formed between the -NO_2 oxygen of **4d** and HIS440, and probably this is the reason why the highest binding affinity was observed for **4d** among all derivatives. It was observed that **4d** interacted with ASN142, CYS145, LEU27, HIS41, ARG188 and MET49, additionally an unfavorable donor-donor interaction was also observed between **4d** and GYL143 amino acid of SARS-CoV-2 M^{pro}. In SARS-CoV-2 M^{pro} – 4d complex, -NO_2 oxygen of **4d** acted as a hydrogen bond acceptor in the formation of an additional hydrogen bond between **4d** and ARG188 amino acid of SARS-CoV-2 M^{pro}. Results showed that all derivatives, including **4d,** interacted with residues in the cat-

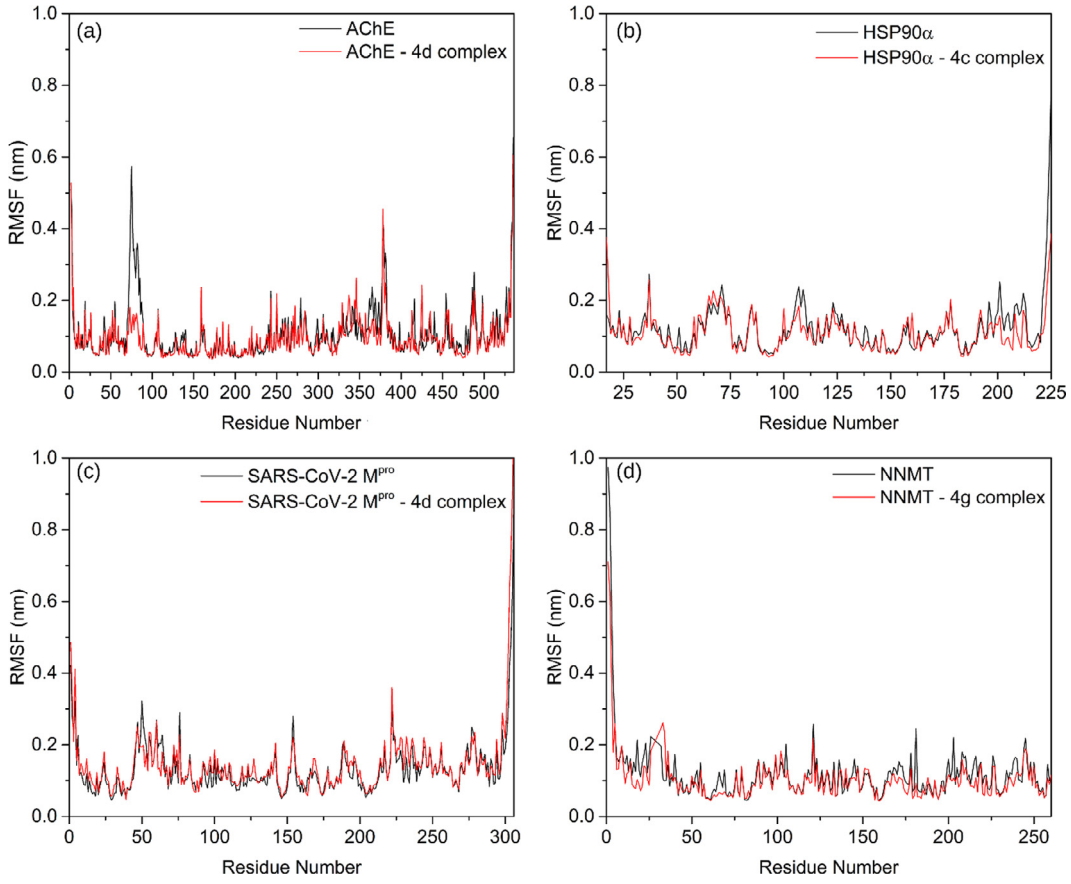

Fig. 15. Results of RMSF analyses of the top-scoring ligand – receptor complexes.

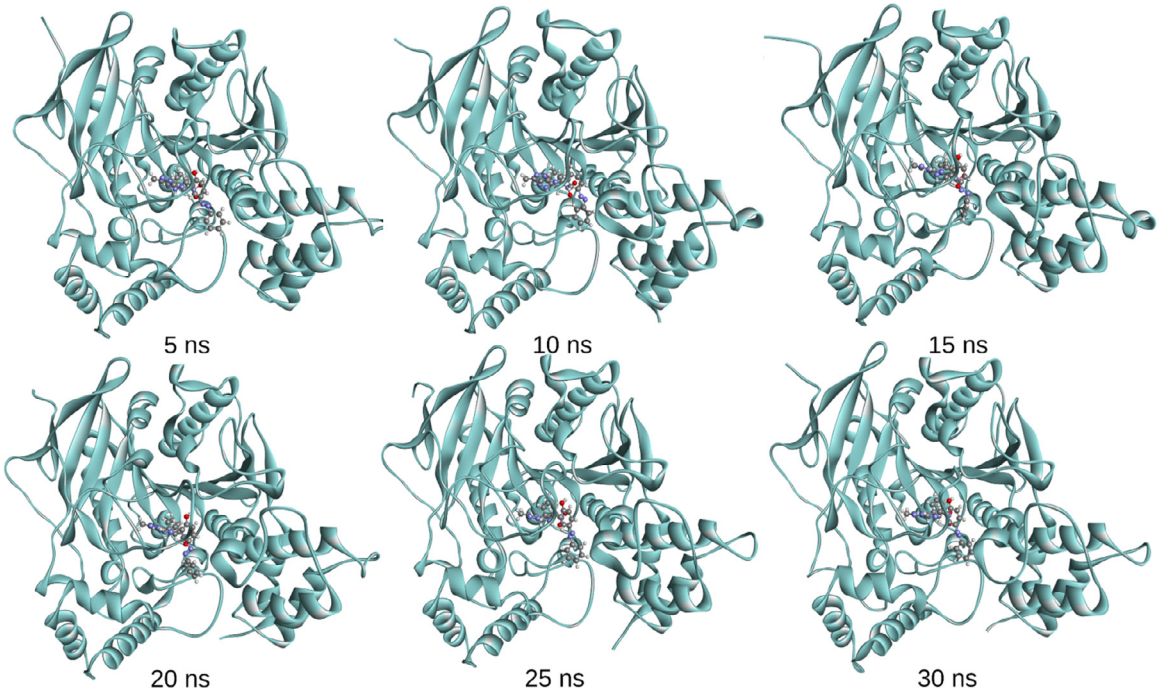

Fig. 16. The structures of 4d - AChE complex recorded at 5, 10, 15, 20, 25 and 30 ns.

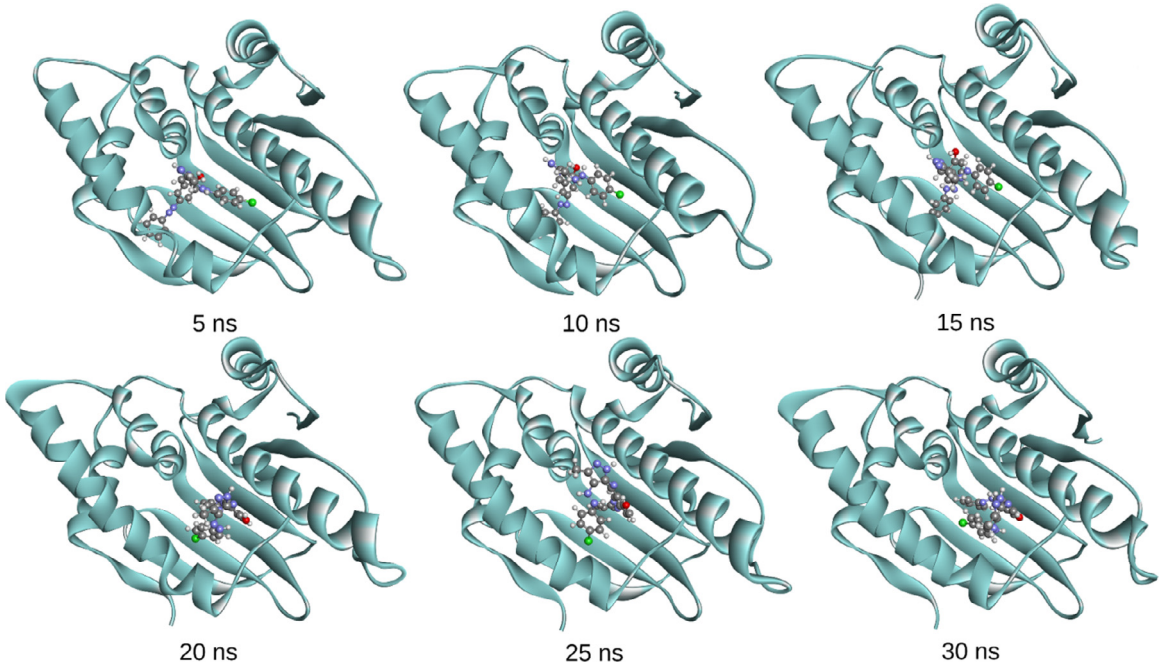

Fig. 17. The structures of 4c - HSP90α complex recorded at 5, 10, 15, 20, 25 and 30 ns.

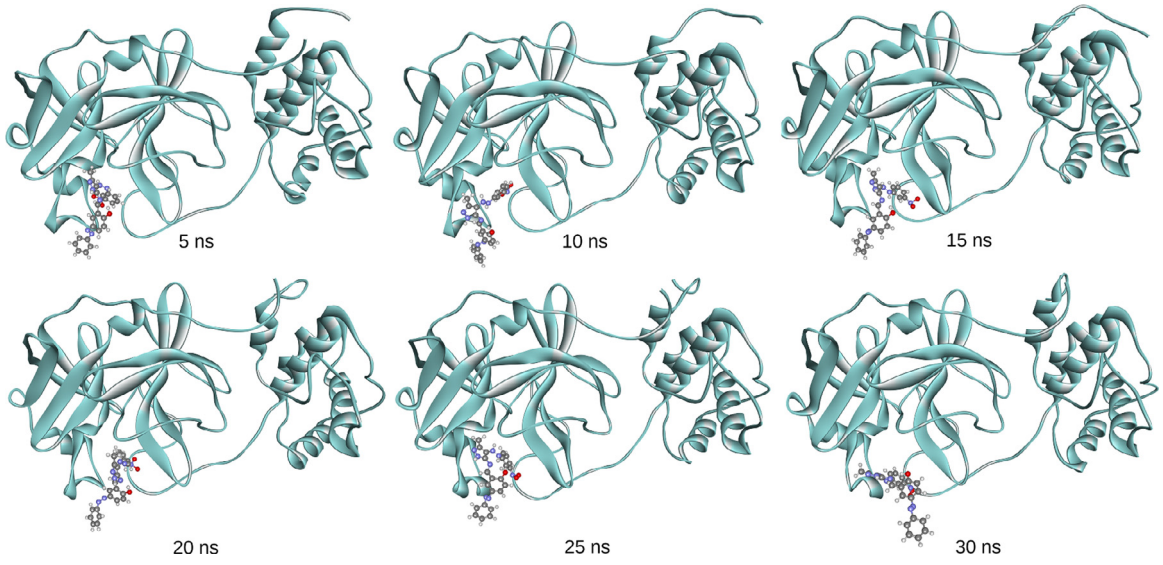

Fig. 18. The structures of 4d - SARS-CoV-2 M^{pro} complex recorded at 5, 10, 15, 20, 25 and 30 ns.

alytic dyad of SARS-CoV-2 M^{pro} (CYS145 and HIS41). In HSP90α – 4c complex, differently from **4a**, chlorine atom at the *para*- position of the phenyl ring took part in the formation of hydrogen bond formed between **4c** and SER52 and alkyl interaction formed between **4c** and VAL186. Results showed that **4c** interacted with ASN51, SER52, VAL186, PHE22, ILE26, TRP162, PHE138 and LEU107 amino acids of HSP90α. In NNMT-4 g complex, it was observed that 4 g interacted with LEU167, TYR204, ALA168, ASN90, ASP85, CYS165, TYR20, TYR24, LYS8, TYR86, CYS141, ALA169, SER7 and VAL143 amino acids of NNMT.

Among all synthesized compounds, **4b**, which has a methoxy group at *para*- position of the phenyl ring possesses the lowest binding affinity in all cases. In Figs. 8–11 molecular docking results are illustrated.

In Fig. 12, comparative representations of the top-scoring synthesized compounds and reference molecules are given. Results showed that all compounds bound to the same binding pocket with corresponding reference molecules. It was observed that in donepezil – AChE and 4d – AChE complexes, TYR334, TYR70 and PHE330; in ganetispib – HSP90α and 4c – HSP90α complexes, LEU107, TRP162 and PHE138; in remdesivir – SARS-CoV-2 M^{pro} and 4d – SARS-CoV-2 M^{pro} complexes, HIS41 and MET49; and lastly in sinefungin – NNMT and 4 g – NNMT complexes, TYR20, CYS165, ASP85, TYR86, ALA168, ALA169 and LYS8 are the common amino acids which took part in the ligand-receptor interactions.

Binding selectivities of the investigated compounds and corresponding targets were calculated and are given in Table 4. In determining the binding selectivities, inhibition constants (K_i) which were calculated by using of Eq. (8) were used. [81] Results showed that all compounds have considerably high selectivity for AChE, HSP90α and especially for NNMT than SARS-CoV-2 M^{pro}. The binding selectivities of all compounds, except 4h, were found to be

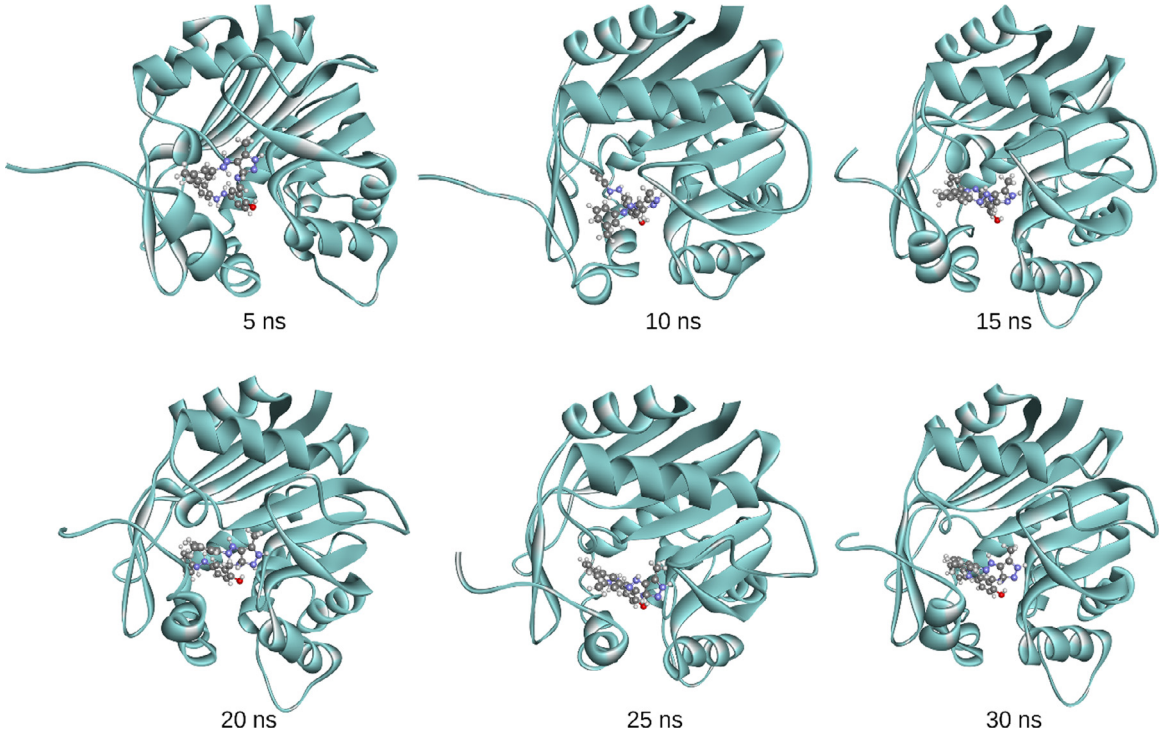

Fig. 19. The structures of 4g - NNMT complex recorded at 5, 10, 15, 20, 25 and 30 ns.

higher for NNMT than HSP90α. Additionally, it was observed that binding selectivities of all compounds, except **4d** and 4h, were found to be higher for NNMT than AChE. On the other hand, a clear trend could not be observed in the relative binding selectivities of the compounds for AChE and HSP90α. For some of the compounds (**4d, 4e, 4f** and 4 g) the binding selectivities for AChE were found to be slightly higher than HSP90α, while for other compounds (**4a** and **4c**), binding selectivities were found to be slightly higher for HSP90α, but in both cases it was observed that they were close to each other.

$$K_i = 10^{BindingEnergy/1.366} \quad (8)$$

3.3.7. Drug-likeness analysis

In this study, Lipinski's rule of five [82] was also used to evaluate drug-likeness of the investigated compounds. Lipinski's rule of five expresses the molecular properties which are important for a drug's pharmacokinetics. Results are given in Table 5. According to Lipinski's rule, a potential drug must have no more than one violation. Results showed that investigated compounds, except **4c, 4d and 4f**, represent no violation of the criteria of Lipinski's rule and compounds that violates the criteria have no more than one violation. logP values of these compounds were found to be slightly higher than the reference value of 5.

3.3.7. Molecular dynamics (MD) simulations

After molecular docking calculations, 30 ns MD simulations were performed on the top-scoring ligand-protein complexes, NNMT – 4 g, AChE – 4d, SARS-CoV-2 M^{pro} – 4d and HSP90α – 4c. MD results of the investigated compounds are given in Supplementary Information.

The root mean square deviation (RMSD) and radius of gyration are indicators for stability of the complexes. In the study, in order to validate the docking poses and the structural stability, RMSD and radius of gyration were assessed. Additionally, the number of hydrogen bonds throughout the MD simulation was monitored.

RMSDs of ligands after least square fit to proteins and RMSDs of protein backbones after least square fit to protein backbones are illustrated in Fig. 13. Results for AChE – 4d complex showed that ligand immediately reached its equilibrium position in the binding pocket and held its position throughout the entire simulation. It was also observed that there was no significant change in the RMSD of protein during the simulation. Results for HSP90α – 4c complex showed that ligand reached its equilibrium position after 15th ns and held its position in the binding pocket in the remaining time of the simulation. Additionally, no significant change was observed in the RMSD of protein during the simulation. Results for SARS-CoV-2 Mpro – 4d complex showed that although there were some changes in the position of the ligand, it remained in the binding pocket throughout the entire the simulation. It was also observed that although there was a slight increase in the RMSD of protein backbone between 16 and 24 ns, it remained stable during the simulation. Lastly, results for NNMT – 4 g complex showed that ligand immediately reached its equilibrium position in the binding pocket and held its position throughout the entire simulation. It was also observed that there was no significant change in the RMSD of protein during the simulation.

Radius of gyration is another effective parameter for investigating the conformational stability and integrity of protein in the ligand – protein complexes. In addition to number of hydrogen bonds formed between ligands and receptors, Rg of the proteins were monitored during the simulation and are given in Fig. 14. Although the changes in the Rg of SARS-CoV-2 M^{pro} were slightly higher than those of AChE, HSP90α and NNMT, it was observed that there were no significant changes in the Rg of proteins. Thus, it was concluded that all proteins remained stable during the MD simulations.

Average Rg values and standard deviations for AChE – 4d, HSP90α – 4c, SARS-CoV-2 M^{pro} – 4d and NNMT – 4 g complexes were found to be 2.3296 nm (0.0054), 1.7252 nm (0.0073), 2.2623 nm (0.0163) and 1.7353 nm (0.0057), respectively. Results also showed that the average number of hydrogen bonds formed

between ligands and receptors were found to be 3.06, 0.70, 0.84 and 1.78 for AChE – 4d, HSP90α – 4c, SARS-CoV-2 M^{pro} – 4d and NNMT – 4 g complexes, respectively. It was observed that the highest number of hydrogen bonds was obtained for AChE – 4d complex and the least one was obtained for HSP90α – 4c complex. Thus, it was concluded that the predominant interactions in the HSP90α – 4c and SARS-CoV-2 M^{pro} – 4d complexes were the interactions other than hydrogen bonds, such as the interactions in which aromatic rings took part.

Root mean square fluctuations (RMSF) of the residues for all top-scoring ligand-receptor complexes are given in Fig. 15. Result of RMSF analyses showed that in AChE – 4d, HSP90α – 4c and NNMT – 4 g complexes, RMSF of the residues located in the binding pocket and took part in the interactions between ligands and receptors were found to be lower than those of the corresponding uninhibited receptors. On the other hand, in SARS-CoV-2 M^{pro} – 4d complex, it was observed that there is no distinct trend in decrease in the RMSF of the residues located in the binding pocket. RMSFs of some certain residues were found to be lower than those of the uninhibited receptor while some of them were found to be higher.

The structures of the top-scoring ligand-protein complexes extracted from the trajectory during the simulation are given in Figs. 16–19. Results showed that investigated ligands were bound to the active site of the corresponding receptor and remained bounded in the binding pocket throughout the entire simulation.

4. Conclusions

A series of 8 novel heterocyclic disperse disazo-azomethine dyes were obtained by the condensation reaction of 5-amino-4-arylazo-3-methyl-*1H*-pyrazoles and 2–hydroxy-5-(phenyldiazenyl) benzaldehyde. Structure characterizations were made by FT-IR and ^{1}H NMR spectra. In addition to those, computational studies were performed. In computational studies, geometry optimizations, frequency analyses, frontier molecular orbital calculations, molecular electrostatic potential map calculations, IR and NMR spectral analyses were performed. The frontier molecular orbital calculations indicated that 4 g, which has the biggest HOMO-LUMO gap, is the most stable compound and on the contrary **4b** has been found as the least stable compound. Molecular docking calculations were also performed to estimate the binding affinities of the investigated compounds for acetylcholinesterase (AChE), heat shock protein (HSP90α), SARS-CoV-2 M^{pro} and NNMT. Although all synthesized compounds have higher binding affinity as reference molecules, for AChE and SARS-CoV-2 M^{pro}, the highest binding affinity values were obtained for **4d** while **4c** possess the highest binding affinity for HSP90α. On the other hand, when the target receptor was NNMT, the highest binding affinity was obtained for 4 g. Among all synthesized compounds, **4b**, which has a methoxy group at *para*- position of the phenyl ring possesses the lowest binding affinity for AChE, HSP90α and SARS-CoV-2 M^{pro} while the lowest binding affinity was observed for 4h in case the target receptor was NNMT. In addition to molecular docking studies the drug-likeness analyses evaluated on **4a-**4h compounds which has no violations except **4c, 4d** and **4f** but these incompatible compounds have only one violation with a slightly higher logP values then the reference value of 5.

Finally, molecular dynamic simulations were evaluated for 30 ns to the best-scoring compounds on reference molecules mentioned above to determine the stability and the flexibility of the ligand - receptor interactions at atomic level. Results showed that in all four complexes, AChE – 4d, HSP90α – 4c, SARS-CoV-2 Mpro – 4d and NNMT – 4 g, ligands effectively bound to the active site of the protein and remained bounded in the binding pocket throughout the entire simulation. Additionally, since no significant change in the RMSD and Rg of the proteins, it was concluded that proteins remained stable during the MD simulations. When the results of these studies are examined, it is possible to say that 4 g, 4**c** and **4d** compounds can be strong candidates in potential drug studies.

Declaration of Competing Interest

The authors declare that they have no known competing financial interests or personal relationships that could have appeared to influence the work reported in this paper.

CRediT authorship contribution statement

Hakki Yasin Odabasoglu: Conceptualization, Writing – original draft. **Taner Erdogan:** Software, Data curation, Investigation, Writing – review & editing. **Fikret Karci:** Conceptualization, Methodology, Supervision.

Acknowledgments

This study has been supported by Pamukkale University Scientific Research Project Coordination Unit by the project number of 2016FBE08. In the computational studies Kocaeli University and TUBITAK ULAKBIM, High Performance and Grid Computing Center (TRUBA) resources were used.

Supplementary materials

Supplementary material associated with this article can be found, in the online version, at doi:10.1016/j.molstruc.2021.131974.

References

[1] Y.D. Kim, J.H. Cho, C.R. Park, J.H. Choi, C. Yoon, J.P. Kim, Synthesis, application and investigation of structure–thermal stability relationships of thermally stable water-soluble azo naphthalene dyes for LCD red color filters, Dyes Pigm. 89 (2011) 1–8.
[2] O.A. Adegoke, T.E. Adesuji, O.E. Thomas, Novel colorimetric sensors for cyanide based on azo-hydrazone tautomeric skeletons, Spectrochim. Acta A Mol. Biomol. Spectrosc. 128 (2014) 147–152.
[3] E. Pevzner, B. Ehrenberg, Principal component analysis of the absorption and resonance Raman spectra of the metallochromic indicator antipyrylazo III, Spectrochim. Acta A Mol. Biomol. Spectrosc. 56 (2000) 637–651.
[4] M. Erfantalab, H. Khanmohammadi, New 1, 2, 4-triazole-based azo–azomethine dye. Part III: synthesis, characterization, thermal property, spectrophotometric and computational studies, Spectrochim. Acta A Mol. Biomol. Spectrosc. 125 (2014) 345–352.
[5] P.J. Coelho, L.M. Carvalho, A.M.C. Fonseca, M.M.M. Raposo, Photochromic properties of thienylpyrrole azo in solution, Tetrahedron Lett. 47 (2006) 3711–3714.
[6] A.Y. Al-Ahmad, Q.M.A. Hassan, H.A. Badran, K.A. Hussain, Investigating some linear and nonlinear optical properties of the azo dye (1-amino-2-hydroxy naphthalin sulfonic acid-[3-(4-*azo*)]-4-amino diphenyl sulfone), Opt. Laser Technol. 44 (2012) 1450–1455.
[7] H. Yousefi, A. Yahyazadeh, E.O. Moradi Rufchahi, M Rassa, Synthesis, spectral properties, biological activity and application of new 4-(benzyloxy)phenol derived azo dyes for polyester fiber dyeing, J. Mol. Liq. 180 (2013) 51–58.
[8] F. Ruyffelaere, V. Nardello, R. Schmidt, J.M. Aubry, Photosensitizing properties and reactivity of aryl azo naphtol dyes towards singlet oxygen, J. Photochem. Photobiol. A Chem. 183 (2006) 98–105.
[9] R. Asgari-sabet, H Khoshsima, Real-time holographic investigation of azo dye diffusion in a nematic liquid crystal host, Dyes Pigm. 87 (2010) 95–99.
[10] J.A. Mikroyannidis, D.V. Tsagkournos, P. Balraju, G.D. Sharma, Low band gap dyes based on 2-styryl-5-phenylazo-pyrrole: synthesis and application for efficient dye-sensitized solar cells, J. Power Sources 196 (2011) 4152–4161.
[11] M.R. Yazdanbakhsh, H. Yousefi, M. Mamaghani, E.O. Moradi, M. Rassa, H. Pouramir, et al., Synthesis, spectral characterization and antimicrobial activity of some new azo dyes derived from 4,6-dihydroxypyrimidine, J. Mol. Liq. 169 (2012) 21–26.
[12] F. Karci, N. Sener, M. Yamac, I. Sener, A. Demircali, The synthesis, antimicrobial activity and absorption characteristics of some novel heterocyclic disazo dyes, Dyes Pigm. 80 (2009) 47–52.
[13] A.Z. Sayed, M.S. Aboul-Fetouh, H.S. Nassar, Synthesis, biological activity and dyeing performance of some novel azo disperse dyes incorporating pyrazolo[1.5-*a*]pyrimidines for dyeing of polyester fabrics, J. Mol. Struct. 1010 (2012) 146–151.
[14] H. Xu, X. Zeng, Synthesis of diaryl-azo derivatives as potential antifungal agents, Bioorg. Med. Chem. Lett. 20 (2010) 4193–4195.

[15] M. Kose, N. Kurtoglu, O. Gumussu, M. Tutak, V. McKee, D. Karakas, et al., Synthesis, characterization and antimicrobial studies of 2-{(E)-[(2-*hydroxy*-5-*methylphenyl*)*imino*]methyl}-4-[(E)-*phenyldiazenyl*]phenol as a novel azo–azomethine dye, J. Mol. Struct. 1053 (2013) 89–99.

[16] H. Khanmohammadi, F. Khodam, Solvatochromic and electrochemical properties of new thermally stable azo–azomethine dyes with $N_2S_2O_2$ donor set of atoms, J. Mol. Liq. 177 (2013) 198–203.

[17] A.E. Taggi, A.M. Hafez, H. Wack, B. Young, D. Ferraris, T. Lectka, The development of the first catalyzed reaction of ketenes and imines: catalytic, asymmetric synthesis of beta-lactams, J. Am. Chem. Soc. 124 (2002) 6626–6635.

[18] S.H. Kim, S.H. Yoon, S.H. Kim, E.M. Han, Red electroluminescent azomethine dyes derived from diaminomaleonitrile, Dyes Pigm. 64 (2005) 45–48.

[19] H.Y. Odabasoglu, Bazi Azometin Boyarmaddelerinin ve Metal Komplekslerinin Yün Kumaslarini Boyama Ozelliklerinin Incelenmesi, Pamukkale University Masters Thesis, Denizli, Turkey, 2012.

[20] R.E. von Kirk, D.F. Othmer, Encyclopedia of Chemical Technology, 12, John Wiley and Sons, 1954 New York, USA.

[21] E. Elizbarashvili, T. Matitaishvili, K. Topuria, Synthesis of macrocyclic polyazomethines, J. Braz. Chem. Soc. 18 (2007) 1254–1258.

[22] X.Y. Li, Y.Q. Wu, D.D. Gu, F.X. Gan, Optical characterization and blu-ray recording properties of metal(II)azo barbituric acid complex films, Mater. Sci. Eng. B 158 (2009) 53–57.

[23] R. Gup, E. Giziroglu, B. Kirkan, Synthesis and spectroscopic properties of new azo-dyes and azo-metal complexes derived from barbituric acid and aminoquinoline, Dyes Pigm. 73 (2007) 40–46, doi:10.1016/j.dyepig.2005.10.005.

[24] S. Wang, S. Shen, H. Xu, Synthesis, spectroscopic and thermal properties of a series of azo metal chelate dyes, Dyes Pigments 44 (3) (2000) 195–198, doi:10.1016/S0143-7208(99)00087-X.

[25] M.S. Refat, I.M. El-Deen, H.K. Ibrahim, S. El-Ghool, Synthesis and spectroscopic studies of some transition metal complexes of a novel Schiff base ligands derived from 5-phenylazo-salicyladehyde and o-amino benzoic acid, Spectrochim. Acta Part A 65 (2006) 1208–1220, doi:10.1016/j.saa.2006.01.049.

[26] K. Nejati, Z. Rezvani, B. Massoumi, Syntheses and investigation of thermal properties of copper complexes with azo-containing Schiff-base dyes, Dyes Pigm. 75 (3) (2007) 653–657.

[27] H. Dincalp, F. Toker, I. Durucasu, N. Avcıbası, S. Icli, New thiophene-based azo ligands containing azomethine group in the main chain for the determination of copper(II) ions, Dyes Pigm. 75 (1) (2007) 11–24, doi:10.1016/j.dyepig.2006.05.015.

[28] Z. Rezvani, A.R. Abbasi, K. Nejati, M. Seyedahmadian, Syntheses, characterization and glass-forming properties of new bis[5-((4-*ndodecyloxyphenyl*)*azo*)-N-(4-*nalkoxyphenyl*)-*salicylaldiminato*]nickel (II) complex homologues, Polyhedron 24 (2005) 1461–1470.

[29] L.D. Popov, Y.P. Tupolova, V.V. Lukov, I.N. Shcherbakov, A.S. Burlov, S.I. Levchenkov, et al., Physico-chemical study of first row transition metal ions coordination compounds with N,N′-bis(2-tosylaminobenzylidene)-1,3-diaminopropanol. The crystal structure of bis-azomethine and its cobalt(II) complex, Inorg. Chim. Acta 362 (2009) 1673–1680.

[30] X. Li, Y. Wu, D. Gu, F. Gan, Spectral, thermal and optical properties of metal(II)–azo complexes for optical recording media, Dyes Pigm. 86 (2) (2010) 182–189.

[31] Z. Jin, X. Du, Y. Xu, Y. Deng, M. Liu, Y. Zhao, et al., Structure of $M^{(pro)}$ from COVID-19 virus and discovery of its inhibitors, Nature 582 (2020) 289–293.

[32] V.N. Holanda, A. de, E.M. Lima, W.V. da Silva, R.T. Maia, R. de L Medeiros, A. Ghosh, et al., Identification of 1,2,3-triazole-phthalimide derivatives as potential drugs against COVID-19: a virtual screening, docking and molecular dynamic study, J. Biomol. Struct. Dyn. (2021) 1–19, doi:10.1080/07391102.2020.1871073.

[33] M.S. Fernandes, F.S. Silva, A.C.S.G. Freitas, E.B. Melo, G.H.G. Trossini, F.R. Paula, Insights on 3D structures of potential drug-targeting proteins of SARS-COV-2: application of cavity search and molecular docking, Mol. Inform. 40 (2021) 2000096 doi:10.1002/minf.202000096.

[34] S.J. Jenepha Mary, S. Pradhan, C James, Molecular structure, NBO analysis of the hydrogen-bonded interactions, spectroscopic (FT–IR, FT–Raman), drug likeness and molecular docking of the novel anti COVID-2 molecule (2E)-N-methyl-2-[(4-*oxo*-4H-*chromen*-3-*yl*)*methylidene*]-hydrazinecarbothioamide (Dimer) - quantum chemical approach, Spectrochim. Acta Part A Mol. Biomol. Spectrosc. 251 (2021) 119388, doi:10.1016/j.saa.2020.119388.

[35] A.A. Alrasheid, M.Y. Babiker, T.A. Awad, Evaluation of certain medicinal plants compounds as new potential inhibitors of novel corona virus (COVID-19) using molecular docking analysis, Silico Pharmaco. 9 (2021) 3, doi:10.1007/s40203-020-00073-8.

[36] N. Sepay, A. Sekar, U.C. Halder, A. Alarifi, M. Afzal, Anti-COVID-19 terpenoid from marine sources: a docking, admet and MD study, J. Mol. Struct. 1228 (2021) 129433, doi:10.1016/j.molstruc.2020.129433.

[37] N. Razzaghi-Asl, A. Ebadi, S. Shahabipour, D. Gholamin, Identification of a potential SARS-CoV2 inhibitor via MD simulations and amino acid decomposition analysis, J. Biomol. Struct. Dyn. (2020), doi:10.1080/07391102.2020.1797536.

[38] G. Garg, A. Khandelwal, B.S.J. Blagg, Anticancer inhibitors of HSP90α function: beyond the usual suspects, Adv. Cancer. Res. (2016) 51–88, doi:10.1016/bs.acr.2015.12.001.

[39] D. Kraus, Q. Yang, D. Kong, A.S. Banks, L. Zhang, J.T. Rodgers, E. Pirinen, T.C. Pulinilkunnil, F. Gong, Y.C. Wang, Y. Cen, A.A. Sauve, J.M. Asara, O.D. Peroni, B.P. Monia, S. Bhanot, L. Alhonen, P. Puigserver, B.B. Kahn, Nicotinamide N-methyltransferase knockdown protects against diet-induced obesity, Nature 508 (2014) 258–262, doi:10.1038/nature13198.

[40] Frisch M.J., Trucks G.W., Schlegel H.B., Scuseria G.E., Robb M.A., Cheeseman J.R., Scalmani G., Barone V., Mennucci B., Petersson G.A., Nakatsuji H., Caricato M., Li X., Hratchian H.P., Izmaylov A.F., Bloino J., Zheng G., Sonnenberg J.L., Hada M., Ehara M., Toyota K., Fukuda R., Hasegawa J., Ishida M., Nakajima T., Honda Y., Kitao O., Nakai H., Vreven T., Montgomery J., Peralta J.E., Ogliaro F., Bearpark M., Heyd J.J., Brothers E., Kudin K.N., Staroverov V.N., Keith T., Kobayashi R., Normand J., Raghavachari K., Rendell A., Burant J.C., Iyengar S.S., Tomasi J., Cossi M., Rega N., Millam J.M., Klene M., Knox J.E., Cross J.B., Bakken V., Adamo C., Jaramillo J., Gomperts R., Stratmann R.E., Yazyev O., Austin A.J., Cammi R., Pomelli C., Ochterski J.W., Martin R.L., Morokuma K., Zakrzewski V.G., Voth G.A., Salvador P., Dannenberg J.J., Dapprich S., Daniels A.D., Farkas O., Foresman J.B., Ortiz J.V., Cioslowski J., Fox D.J., Gaussian 09 (Version 9.5). 2013, Gaussian Inc.: Wallingford CT.

[41] C.E. Chang, M.K. Gilson, Tork: conformational analysis method for molecules and complexes, J. Comput. Chem. 24 (16) (2003) 1987–1998, doi:10.1002/jcc.10325.

[42] Dennington R., Keith T., Millam J., GaussView 5 (Version 5.0.9). 2009, Semichem Inc.: Shawnee Mission, KS.

[43] D.S. Biovia, Discovery Studio Visualizer (Version 20.1.0.19295) 2020, Dassault Systèmes, San Diego.

[44] G.M. Morris, R. Huey, W. Lindstrom, M.F. Sanner, R.K. Belew, D.S. Goodsell, A.J. Olson, AutoDock4 and AutoDockTools4: automated docking with selective receptor flexibility, J. Comput. Chem. 30 (16) (2009) 2785–2791.

[45] O. Trott, A.J. Olson, AutoDock Vina, Improving the speed and accuracy of docking with a new scoring function, efficient optimization, and multithreading, J. Comput. Chem. 31 (2) (2010) 455–461.

[46] G. Kryger, I. Silman, J.L. Sussman, Structure of acetylcholinesterase complexed with E2020 (Aricept): implications for the design of new anti-Alzheimer drugs, Structure 7 (3) (1999) 297–307.

[47] H.M. Berman, J. Westbrook, Z. Feng, G. Gilliland, T.N. Bhat, H. Weissig, I.N. Shindyalov, P.E. Bourne, The Protein Data Bank, Nucleic Acids Res 28 (2000) 235–242.

[48] J. Shi, R. Van de Water, K. Hong, R.B. Lamer, K.W. Weichert, C.M. Sandoval, et al., EC144 is a potent inhibitor of the heat shock protein 90, J. Med. Chem. 55 (17) (2012) 7786–7795.

[49] S. Kim, J. Chen, T. Cheng, A. Gindulyte, J. He, S. He, et al., PubChem 2019 update: improved access to chemical data, Nucl. Acids Res. 47 (D1) (2018) D1102–D1109.

[50] T. Sterling, J.J. Irwin, ZINC 15 – Ligand discovery for everyone, J. Chem. Inf. Model. 55 (11) (2015) 2324–2337.

[51] P.A. Ravindranath, S. Forli, D.S. Goodsell, A.J. Olson, M.F. Sanner, AutoDockFR: Advances in Protein-Ligand Docking with Explicitly Specified Binding Site Flexibility, PLOS Comput. Biol. 11 (2015) e1004586 https://doi.org/10.1371/JOURNAL.PCBI.1004586.

[52] F. Wang, F.X. Wu, C.Z. Li, C.Y. Jia, S.W. Su, G.F. Hao, G.F. Yang, ACID: a free tool for drug repurposing using consensus inverse docking strategy, J. Cheminform 11 (2019) 1–11, doi:10.1186/s13321-019-0394-z.

[53] Drug Likeness Tool (DruLiTo). http://www.niper.gov.in/pi_dev_tools/DruLiToWeb/DruLiTo_index.html, 2020 (accessed 10 March 2020).

[54] D. Van der Spoel, E. Lindahl, B. Hess, G. Groenhof, A.E. Mark, H.J.C. Berendsen, GROMACS: fast, flexible, and free, J. Comput. Chem. 26 (2005) 1701–1718, doi:10.1002/jcc.20291.

[55] R.B. Best, X. Zhu, J. Shim, P.E.M. Lopes, J. Mittal, M. Feig, et al., Optimization of the additive CHARMM all-atom protein force field targeting improved sampling of the backbone φ, ψ and side-chain $\chi 1$ and $\chi 2$ dihedral angles, J. Chem. Theory Comput. 8 (2012) 3257–3273, doi:10.1021/ct300400x.

[56] V. Zoete, M.A. Cuendet, A. Grosdidier, O. Michielin, SwissParam: a fast force field generation tool for small organic molecules, J. Comput. Chem. 32 (2011) 2359–2368, doi:10.1002/jcc.21816.

[57] M.H. Elnagdi, M.M.M. Sallam, H.M. Fahmy, S.A.M. Ibrahim, M.A.M. Elias, Reactions with the arylhydrazones of-cyanoketones: the structure of 2-arylhydrazone-3-ketimino-nitriles, Helv. Chim. Acta 59 (1976) 551–557.

[58] M.H. Elnagdi, G.E.H. Elgemeie, F.A.E. Abdelaal, Recent developments in the synthesis of pyrazole derivatives, Heterocycles 23 (12) (1985) 3121–3153.

[59] M. Odabasoglu, C. Albayrak, R. Ozkanca, F.Z. Aykan, P. Lonecke, Some polyhydroxy azo–azomethine derivatives of salicylaldehyde: synthesis, characterization, spectroscopic, molecular structure and antimicrobial activity studies, J. Mol. Struc. 840 (2007) 71–89.

[60] F. Karci, A. Demircali, Synthesis of disazo pyrazolo[1,5-*a*]pyrimidines, Dyes Pigm. 74 (2007) 288–297.

[61] Z.J. Mohamed, A.H. Al-Khafagy, Characterization and biological study of heterocyclic azo-schiff base compound and some of its metal complexes, Int J Curr Res 5 (12) (2013) 3705–3710.

[62] T. Koopmans, Über die zuordnung von wellenfunktionen und eigenwerten zu den einzelnen elektronen eines atoms, Physica 1 (1) (1934) 104–113 German.

[63] P.K. Chattaraj, U. Sarkar, R.D. Roy, Electrophilicity index, Chem. Rev. 106 (6) (2006) 2065–2091.

[64] R.S. Mulliken, A new electroaffinity scale: together with data on valence states and on valence ionization potentials and electron affinities, J. Chem. Phys. 2 (1934) 782.

[65] R.G. Parr, R.G. Pearson, Absolute hardness-companion parameter to absolute electronegativity, J. Am. Chem. Soc. 105 (26) (1983) 7512–7516.

[66] R.G. Parr, L. von Szentpaly, S.B Liu, Electrophilicity index, J. Am. Chem. Soc. 121 (9) (1999) 1922–1924.
[67] R.G. Pearson, Hard and soft acids and bases, J. Am. Chem. Soc. 85 (22) (1963) 3533–3539.
[68] R.G. Pearson, Hard and soft acids and bases HSAB.1.Fundamental principles, J. Chem. Educ. 45 (9) (1968) 581.
[69] R.G. Pearson, Maximum chemical and physical hardness, J. Chem. Educ. 76 (2) (1999) 267–275.
[70] B.R. Beck, B. Shin, Y. Choi, S. Park, K. Kang, Predicting commercially available antiviral drugs that may act on the novel coronavirus (SARS-CoV-2) through a drug-target interaction deep learning model, Comput. Struct. Biotechnol. J. 18 (2020) 784–790.
[71] D.C. Hall, Ji H-F, A search for medications to treat COVID-19 via in silico molecular docking models of the SARS-CoV-2 spike glycoprotein and 3CL protease, Travel Med. Infect. Dis. (2020) 101646.
[72] M. Macchiagodena, M. Pagliai, P. Procacci, Identification of potential binders of the main protease 3CLpro of the COVID-19 via structure-based ligand design and molecular modeling, Chem. Phys. Lett. (2020) 137489.
[73] B. Robson, Computers and viral diseases. Preliminary bioinformatics studies on the design of a synthetic vaccine and a preventative peptidomimetic antagonist against the SARS-CoV-2 (2019-nCoV, COVID-19) coronavirus, Comput. Biol. Med. 119 (2020) 103670.
[74] C. Wu, Y. Liu, Y. Yang, P. Zhang, W. Zhong, Y. Wang, et al., Analysis of therapeutic targets for SARS-CoV-2 and discovery of potential drugs by computational methods, Acta Pharm. Sin. B 10 (5) (2020) 766–788, doi:10.1016/j.apsb.2020.02.008.
[75] P.K. Parida, D. Paul, D. Chakravorty, The natural way forward: MD simulation analysis of phytochemicals from Indian medicinal plants as potential inhibitors of SARS-CoV-2 targets, Phytother. Res. (2020) 1–14, doi:10.1002/ptr.6868 10.1039/d0ra07062a.
[76] D.A. Milenković, D.S. Dimić, E.H. Avdović, Z.S. Marković, Several coumarin derivatives and their Pd(II) complexes as potential inhibitors of the main protease of SARS-CoV-2, an in silicoapproach, RSC Adv. 10 (58) (2020) 35099–35108, doi:10.1039/d0ra07062a.
[77] P. Rao, A. Shukla, P. Parmar, R.M. Rawal, B. Patel, M. Saraf, et al., Reckoning a fungal metabolite, Pyranonigrin A as a potential main protease (M^{pro}) inhibitor of novel SARS-CoV-2 virus identified using docking and MD simulation, Biophys. Chem. 264 (2020) 106425, doi:10.1016/j.bpc.2020.106425.
[78] K.A. Peele, C. Potla Durthi, T. Srihansa, S. Krupanidhi, V.S. Ayyagari, D.J. Babu, et al., Molecular docking and dynamic simulations for antiviral compounds against SARS-CoV-2: a computational study, Inform. Med. Unlocked 19 (2020) 100345, doi:10.1016/j.imu.2020.100345.
[79] D.S.N.B.K. Prasanth, M. Murahari, V. Chandramohan, S.P. Panda, L.R. Atmakuri, C. Guntupalli, In silico identification of potential inhibitors from Cinnamon against main protease and spike glycoprotein of SARS CoV-2, J. Biomol. Struct. Dyn. (2020) 1–15, doi:10.1080/07391102.2020.1779129.
[80] K. Al-Khafaji, D. Al-Duhaidahawi, T.T. Tok, Using integrated computational approaches to identify safe and rapid treatment for SARS-CoV-2, J. Biomol. Struct. Dyn. (2020) 1–9, doi:10.1080/07391102.2020.1764392.
[81] A.T. Onawole, T.U. Kolapo, K.O. Sulaiman, R.O. Adegoke, Structure based virtual screening of the Ebola virus trimeric glycoprotein using consensus scoring, Comput. Biol. Chem. 72 (2018) 170–180, doi:10.1016/J.COMPBIOLCHEM.2017.11.006.
[82] C.A. Lipinski, F. Lombardo, B.W. Dominy, P.J. Feeney, Experimental and computational approaches to estimate solubility and permeability in drug discovery and development settings, Adv. Drug Deliv. Rev. 23 (1) (1997) 3–25.